Role of Serum Albumin Aggregation in Lubrication and Wear Protection of Shearing Surfaces

By

Mihir Samak

Thesis submitted in partial fulfillment of the requirements for

Master of Applied Science

in

Biomedical Engineering

FACULTY OF ENGINEERING

UNIVERSITY OF OTTAWA

(Thesis done under the Dept. of Physics)

Abstract

Healthy articular joints exhibit remarkable lubrication due in large part to the complex rheological and tribological behavior of the synovial fluid (SF) that lubricates the joints. Current approaches that seek to elucidate such remarkable lubrication usually focus on the roles of high molecular weight SF components such as lubricin and hyaluronic acid but frequently overlook the role of serum albumin (SA), although it represents 90% of the protein content of SF. In this thesis, we used the Surface Forces Apparatus to investigate in detail the structural and tribological response of SA thin films when sheared between model surfaces and subjected to a large range of shearing parameters. Our data indicate that, under shear, SA films reproduce closely the shear response previously reported for SF, i.e., film thickening and formation of numerous long-lived aggregates accompanied by low friction and efficient surface protection against damage. More specifically, our detailed investigation of shear parameters reveals that (i) strong anchoring of SA to surfaces promotes the formation of large rod-like shaped aggregates that enable rolling friction and keep surfaces far apart, preventing damage, (ii) aggregation mechanism is irreversible, which makes aggregates long-lived (though mobile) in the contact, and (iii) aggregate formation only occur when SA was sheared above a 'critical' amplitude A_c and a critical shear velocity V_c.

Collectively, our results provide experimental evidence of the role of globular proteins, such as SA, in lubrication and establish a correlation between shearing parameters, formation and stability of aggregates, low friction and wear protection. Although our findings are based on experiments involving rigid, nonporous surfaces hence can hardly be generalized to compliant and porous cartilage surfaces, they are applicable to other rigid tribosystems such as artificial joints and will certainly advance our understanding of joint implants' lubrication in SF mediated by protein aggregation, with implications for future design of artificial joints and therapeutic interventions.

Table of Contents

List of Figures

List of Tables

List of Abbreviations

SA	Serum Albumin
FN	Fibronectin
SF	Synovial Fluid
OA	Osteoarthritis
ECM	Extracellular Matrix
LUB	Lubricin
LS	Laminar Splendens
V_{shear}	Shearing Velocity
EHL	Elastohydrodynamic Lubrication
TFL	Thick Film Lubrication
HA	Hyaluronic Acid
PBS	Phosphate Buffer Saline
CoCrMo	Cobalt Chromium Molybdenum
UHMWPE	Ultra High Molecular Weight Polyethylene
SZP	Superficial Zone Protein
PL	Phospholipids
BSA	Bovine Serum Albumin
SFA	Surface Forces Apparatus
AFM	Atomic Force Microscopy
DP	Dispersion
FECO	Fringes of Equal Chromatic Order
P1	Protocol 1
P2	Protocol 2
P3	Protocol 3
P4	Protocol 4
FBS	Fetal Bovine Serum

To my late uncle Col. Uday Vidwans,

who believed in me

Acknowledgement

Firstly, I would like to thank my supervisor Dr. Delphine Gourdon for giving me the opportunity to work under her, and for all the support and guidance she gave me throughout my research. I would also like to thank my wonderful colleagues Dr. Elie Ngandu Mpoyi, Maryam Asadishekari, Halimo Aden, Naveena Janakiraman, and Parisa Sadeghi, without whom I wouldn't have been able to accomplish my goals. Their constant support and guidance helped me to stay focus. All of you guys made my lab experience worth cherishing.

My special thanks to Kate Lerigoleur and Sierra Cook for teaching me the essentials of Surface Forces Apparatus, and for being patient with all my mistakes. Also, to Mr. Hemant Urdhwareshe for his guidance in my statistical analysis. It wouldn't have been possible without his expertise.

I would also like to extend a special thanks to my guru Lt. Col. A.K. Singh who taught me the core values of becoming a gentleman and an officer, and for always being there for my support. His training helped me shape my way of thinking and inculcated a sense of leadership, and I will always be grateful to him.

And lastly, this journey wouldn't have taken shape without the constant support of my family and friends. I thank my parents for supporting me financially and believing in my decisions. My awesome and evergreen grandparents who always encouraged me to work hard, my sister and my brother-in-law for being a huge support, my loving uncle Reuben and my aunt Jessica, my supportive cousins Liron and Baaram, and my amazing friends who made sure I never wavered off from my path.

I dedicate this thesis to my family, friends, and all the diligent chondrocytes and the synovial proteins that work really hard in giving us the ability to articulate.

This work was supported financially by a Natural Sciences and Engineering Research Council of Canada (NSERC) Discovery Grant under award RGPIN-2017-06784 (to Delphine Gourdon).

Chapter - I : Introduction

1.1 Overview and Motivation:

Healthy articular joints exhibit highly efficient lubrication, characterized by extremely low friction coefficients accompanied by strong resistance to wear. Together with cartilage composition and structure, the rheological and tribological characteristics of synovial fluid (SF) provide the necessary conditions for this exceptional lubrication. SF comprises multiple components that were reported to contribute either individually or synergistically to the lubrication of cartilage surfaces [1][2]. In 2014, it was observed that when SF is sheared between rigid (mica) surfaces, it undergoes a sudden increase in film thickness and forms agglomerates [3]. These agglomerates are able to roll within the sheared junction and keep the surfaces apart, even under high loads, by behaving as ball bearings [3]. Recently, we discovered that, among all SF constituents, serum albumin (SA) is a key contributor to shear-mediated aggregates formation [2], however the parameters responsible for aggregation, the lifetime of aggregates and their exact role in lubrication are still unclear. In this thesis, we propose to use the Surface Forces Apparatus (SFA) to (i) study the dynamics of formation of aggregates in SA films under shear and (ii) correlate aggregates properties with friction forces and wear resistance of sheared surfaces. A detailed description of all the parameters we tested can be found in Section 1.5.

In osteoarthritis (OA), the composition of SF is affected by alterations taking place in the fluid itself and in the surrounding synovial joint tissues, which in turn deteriorate SF rheological properties, thereby affecting its ability to lubricate the surfaces effectively [1][4][10]. For example, both the concentration and the molecular weight of hyaluronic acid (HA) are lower in the SF associated with OA compared to healthy joints, further resulting in lowering the viscosity and affecting the rheological properties of osteoarthritic SF [1][4]. While lubricin (LUB) concentration was also reported to decrease in OA SF, phospholipids (PL) concentration was seen to increase thereby affecting SF's boundary lubricating properties [1]. Protein overall concentration in SF is also altered due to OA. It was quantified on the higher side in most OA patients, which was indicative of changes taking place in the synovium with respect to its functions and structure due to inflammation [10]. This pathological condition (OA) further degenerates the cartilage due to insufficient lubrication and an increase in friction, which is an irreversible change. Keeping these diseased joints well lubricated at the onset of OA by the use of biomimetic lubricants through various supplementary methods, such as oral

or intra-articular injections, may help in delaying its devastating effects on those suffering from it.

Current approaches that seek to elucidate SF remarkable lubrication usually focus on the roles of high molecular weight SF components such as hyaluronic acid and lubricin [5][6] but frequently overlook the role of albumin, although it represents 90% of the protein content of SF. However, the protective role of SA has been previously demonstrated in artificial joints, in particular its ability to prevent wear of implants surface by providing good boundary lubrication, thereby reducing friction [5][6]. When prosthetic materials such as cobalt chromium molybdenum (CoCrMo) alloy, stainless steel, and ultra high molecular weight polyethylene (UHMWPE) were subjected to lubricants containing SA, these lubricants demonstrated their ability to avoid adhesion and accumulation of wear debris originating from damaged sheared surfaces. Biomimetic lubricants with not only good lubricating properties but also better protective capabilities can prove highly beneficial to patients suffering from OA. On the other hand, if patients need joints replacement, the identification of a shear-induced lubricating mechanism of SF, mediated by the aggregation of globular proteins such as SA, will advance our current understanding of joint implants' lubrication with implications for future design and therapeutic interventions.

1.2 Physiology of Healthy Synovial Joints:

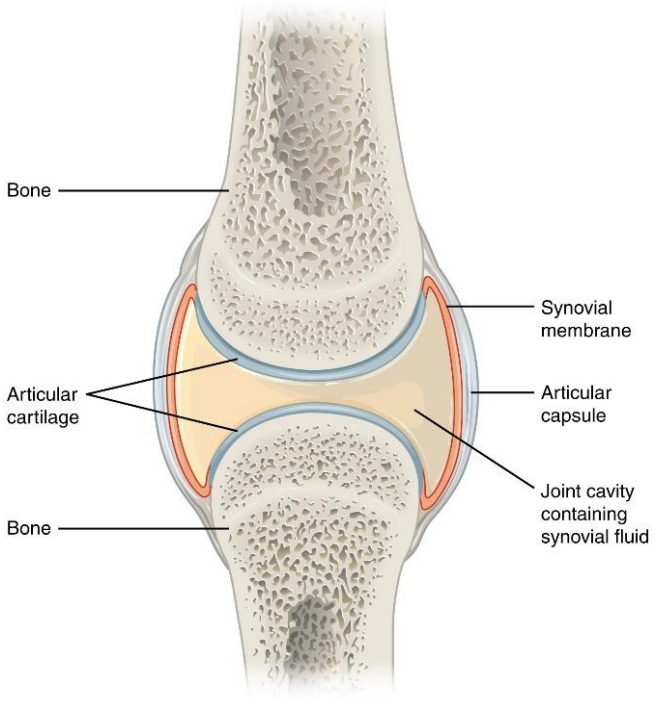

Fig. 1.2.1 Synovial joint diagram [www.opentextbc.ca]

Human joints can broadly be distinguished into three categories – synarthrosis or the immovable joint; mixed articulation joints; and diarthrosis or the synovial joint, which articulates to allow free movement. Synovial joints, hence, are a crucial part of a mammalian lifespan as they permit movement and locomotion, fundamental functions of the skeleton. As seen in Fig. 1.2.1, synovial joints are composed of an articular cartilage that forms a covering layer for the opposing skeletal components; SF that works as a lubricant and a protective film against frictional damage; the articular capsule that provides insulation and seals the joint space from surrounding tissues; the synovial membrane or synovium that forms the inner membrane of the articular capsule and majorly contributes to the production of the SF; and ligaments that provide the necessary stability during movement. Efficient lubricating properties of healthy synovial joints assist in both ensuring low friction and resisting wear even after being subjected to over 100 million shearing cycles in an average lifespan of a human [2].

1.2.1 Articular Cartilage:

The articular cartilage is a biphasic hyaline cartilage, composed of a fluid phase and a solid phase, covering the bones in the synovial joint [8]. It is a specialised tissue whose principal functions are to provide a smooth load bearing surface for articulation, shock absorption and transmission of loads while maintaining a very low coefficient of friction [8][9]. It is a smooth slippery whitish tissue forming a 1 to 4 mm thick layer over the opposing bones, devoid of nerves, lymphatics, and blood vessels. It comprises a dense, permeable, porous extracellular matrix (ECM) primarily composed of collagen and proteoglycans that are surrounded by water, which symbiotically contribute to maintaining the hydration of the ECM and preserve its mechanical properties [8]. The ECM also scantily houses specialised cells called chondrocytes, which are the only cells found in the cartilage, forming about 2% of its total volume. Chondrocytes are responsible for the development and maintenance of the ECM, and are crucial in the well being of the joint. However, their restricted proliferative capability is responsible for the inherent inability of cartilage to heal post injury [8]. These cells are sensitive to mechanical loads and follow the process of mechanotransduction for their cellular activities. Hence, their viability and proper function depend on normal stresses in an optimal mechanical environment [8][9].

As schematized in Fig. 1.2.2, there are in general four distinct zones in the articular cartilage namely the superficial zone, the middle zone, the deep zone, and the calcified zone [8][9]. The thin superficial zone is composed of a large number of flattened chondrocytes and a fibrillar mesh where the type II collagen fibres are tightly coupled together and parallelly

positioned to the articular surface [8][9]. This zone is responsible for providing low friction at boundary level during articulation, and for facilitating the necessary tensile strength to the cartilage whilst protecting the deeper layers. It is in direct contact with SF and enables the cartilage to provide resistance to compressive forces exerted during articulation [8]. The fibrillar tightly connected network of the type II collagen entangles negatively charged proteoglycans. Additionally, highly polar water molecules are attracted towards these proteoglycans thus creating a channel for water to fill in the tissue. Together with the tight mesh of collagen fibrils, proteoglycans and water enable the superficial zone to sustain the compressive forces exerted on the cartilage [34]. The middle zone comprises about 40% to 60% of the total volume of the cartilage, and the collagen in this zone is obliquely arranged. The role of this zone is to oppose the compressive forces inflicted during movement. The deep zone is composed of collagen fibres aligned perpendicular to the articular surface and it provides the necessary resistance to loads acting on it. The fibres in this deep zone have a larger diameter than those in all other zones of cartilage [8]. Finally, the calcified zone bridges the cartilage to the bone by facilitating firm attachment of the deep zone collagen fibres to the subchondral bone.

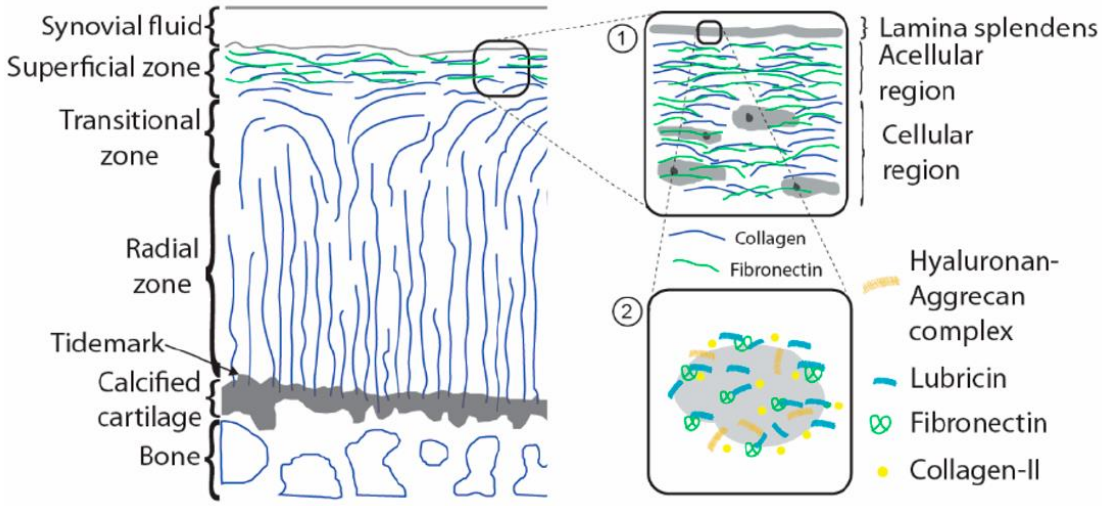

Fig. 1.2.2 Structure and composition of articular cartilage [7]

1.2.2 Synovium:

The synovium, a thin tissue lining the inner part of the articular capsule, is composed of synoviocytes which can be either fibroblastic (type B) or macrophagic (type A) [10]. It acts as a semipermeable membrane for exchange of specific size of solutes and seals off the SF from the surrounding tissue thereby effectively preventing the SF from getting squeezed out from the junction. This helps to keep the joint lubricated and not run dry when it is subjected

to pressure and shear. It efficiently provides a fencing mechanism for the transport of molecules in SF and plasma to and from the synovial joint [10].

Apart from confining SF within the joint cavity, one of the main responsibilities of the synovium is to contribute to the formation of SF. It provides the necessary environment for the transfer of an ultrafiltrate of blood plasma through its capillary walls into the joint cavity [10]. This plasma in conglomeration with hyaluronan synthesized by the type B synoviocytes of the membrane, and various other proteins produced by the surrounding tissue, forms the synovial fluid [11]. Additionally, the synovium allows for the transport of nutrients to the articular cartilage that has no direct supply of nutrients (due to its avascular nature), and this nutrition transpires through diffusion from SF [8]. The role of SF is further discussed in the following section.

1.3 Role of Synovial Fluid and its Components in Healthy Joints:

1.3.1 Synovial Fluid:

SF is a pale-yellow liquid responsible for lubrication and protection of the articular cartilage, as the opposing surfaces constantly get in contact during articulation. SF is derived from an ultrafiltrate of blood plasma, proteins synthesized by the synovium, the articular cartilage, and the surrounding tissues [10][11]. It mainly consists of HA, LUB (also called superficial zone protein (SZP)), SA, and surface-active PL [10][12]. In humans, a healthy knee joint contains approximately 1 mL of SF [10]. Few of the important principal functionalities of SF are to (i) ensure low friction and wear protection of the articulating surfaces under a large range of pressures and shear conditions, (ii) supply the necessary nutrients to the cartilage, and (iii) mediate communication between cells in the joints [8][10][13]. SF displays extremely low coefficients of friction, in the range of 0.002 to 0.01 for bovine SF [4]. This feature of SF helps maintain the opposing articular surfaces' lubricity and protect them from abrasion for several decades. SF is also responsible for facilitating removal of metabolic waste products and transporting other metabolites into and out of the synovial cavity [8][11].

While the multiple functions of SF are well understood thanks to the intensive research that has been taking place since the 20th century, how it functions as such an efficient lubricant is still unclear [4][11]. Indeed, some ambiguity remains in explaining the individual and/or synergistic roles of the various SF components in lubrication. However, there is a general consensus that LUB, HA, and PL are the major contributors to the remarkable lubricating properties of SF [9] [12][13]. The role of SA, on the other hand, has been elusive and not much

has been reported about its contributions to articular lubrication [4]. The rheological characteristics of SF proteins were studied by Tirtaatmadja *et al.* in 1984, and it was observed that globular proteins, in conjunction with HA, contributed greatly to the mechanical behaviour of SF [14]. Their study concluded that proteins significantly affect the rheological properties of SF, which was recently confirmed by results obtained in our lab on both SF and SA thin films sheared between rigid surfaces [2]. Additionally, Oates *et al.* reported aggregates in SF, which strongly influenced its viscoelasticity [4]. These studies provide a reasonable premise for researchers to look deeper into the role of protein aggregation in articular lubrication, in particular the role of SA, as discussed in Section 1.4.

1.3.2 Hyaluronic Acid:

Hyaluronic acid (HA), also called hyaluronan, is a high molecular weight (6-7 MDa) non-sulphated glycosaminoglycan, and is one of the most abundant components found in SF [10][15]. It appears as a nonuniform dispersion and its concentration in SF ranges from 1 to 4 mg/ml [10][12][15]. HA is considered to responsible for the high viscosity of SF [10][15][16]. It is also considered as a key constituent of SF for its boundary lubricating ability [2][17][18]. In fact, in pathological conditions of the joint, especially in OA, the rheology of HA is affected through depolymerisation of the high molecular weight glycosaminoglycan to low molecular weight by-products [18]. Also, HA concentration is significantly lower in pathological SF [10]. These findings promoted the development of HA-based therapeutics for OA patients. These treatments showed (short term) positive results when it came to cartilage lubrication, chondroprotective abilities, reducing articular inflammation, or acting as an analgesic [17].

However, there has been some ambiguity in considering HA as one of the main contributors to cartilage lubrication, as contradicting results have been shown in recent studies [2][17][18]. Specifically, HA was reported to have insignificant loadbearing abilities, and removal of HA by using hyaluronidase, enzymes that can digest HA, showed no effect on the lubricating behaviour of SF [18]. The beneficial effects of HA-based therapeutic modalities too were not uniformly observed through populations of arthritic patients [17]. In fact, guidelines from both the American College of Rheumatology and the Osteoarthritis Research Society International have remained neutral on the necessity of HA based treatments due to variable conclusions obtained from clinical studies [17].

1.3.3 Lubricin:

Besides HA, LUB has also been identified as an effective boundary lubricating component of SF [2][18][19]. LUB is a high molecular weight glycoprotein displaying a bottle-

brush like configuration with a concentration of 0.2 mg/ml in SF [18]. It has a large highly hydrophilic mucin region that helps retaining water molecules at the cartilage surface, which ensures a low coefficient of friction at the cartilage surface [18]. It is principally synthesized by the superficial zone chondrocytes, and hence also called superficial zone protein (SZP) [19]. In healthy articular joints, it plays a pivotal role in maintaining the lubricity at the interface between cartilage and SF [19]. It was also reported as a chondroprotective, and proliferation regulatory agent [19]. Its depletion has been observed most osteoarthritis patients' SF [19].

Despite the existence of a plethora of non-operative therapeutic remedies available for OA, their effectiveness in limiting its prognosis is minimal [17][19]. While some studies have shown the effectiveness of visco-supplementary injections based on HA and LUB, there still exists a controversial debate in their potency [17]. There is still a need to find novel biomimetic fluids that would not only be an effective lubricant but also possess a good wear-protective capability for a long-lasting effect. These biomimetics would prove highly beneficial in controlling OA, and giving a much-needed pain-relief to its patients.

1.3.4 Lamina Splendens:

Although it is still under debate, the articular cartilage surface or the superficial zone is thought to be covered by a gel-like layer, usually referred to as *lamina splendens* (LS). This layer comprises the same constituents than SF, but at much higher concentrations [3]. LS is believed to form a 250-500 nm thick transient layer at the interface between the cartilage and SF [20]. It is afibrillar, it contains high amounts of PL, HA, and LUB, but also other proteins such as fibronectin or non fibrillar collagen II, and is loosely connected to the underlying cartilage surface [3][20][21]. Not much is known about its composition or molecular structure, but its formation was suggested to be mediated by shearing of SF [3]. In their study, Banquy *et. al.* show that SF forms an aggregate gel-like layer when it is subjected to normal force and sheared (at low shearing velocities) between rigid surfaces [3]. The authors also indicate that, although it is fragile, this layer is steady over time, localised exclusively at regions previously sheared, and associated with a remarkable local increase in SF film thickness.

While there are contradicting reports about the role of LS in boundary lubrication, most studies have considered it to be an *active* contributor to joint lubrication. This fragile layer, even when is abraded, is suggested to form small particles that help to keep the surfaces apart by getting localised in the junction and work like ball bearings [3]. However, it is remains unclear as to which SF constituents contributes to its formation and sustainability. As our recent study [2] suggests that SA plays a key role in SF's ability to undergo a sudden increase in film

thickness and agglomerates formation, this motivated us to elucidate further the mechanisms responsible for the shear-induced transformation of SA. Our findings will further help in providing an insight into the role of globular proteins (such as SA) in SF lubrication by establishing a correlation between shear-mediated aggregates' (also called gel layer) formation, low friction and surface protection against wear. Although it will be of future interest to investigate these aggregation phenomena between cartilage surfaces, the results we obtained using rigid model surfaces will certainly advance our understanding of joint implants' lubrication with implications for future design of artificial joints and therapeutic interventions.

1.4 Role of Serum Albumin in Lubrication:

1.4.1 Overview and Molecular Structure:

SA is considered as the most versatile transport protein in a human body [22]. It is profusely found in the mammalian circulatory system, and is synthesized by the liver [23]. It has remarkable binding abilities and shares a high affinity for various drugs and organic compounds [23]. Out of the total weight of the protein content of SF, SA represents about 90% [2][24]. As seen in Fig. 1.4.1, it has a heart-shaped folded structure consisting of three repeating domains, namely I, II, and III, and a molecular weight of circa 66 kDa [4][23][25]. Each domain is further divided into two sub-domains [23][25]. SA's radius of gyration is about 3.5 nm [4] and it comprises almost 67% α-Helical [23] with no β-sheet [26] secondary structures. Concentration of SA in SF ranges from 7 to [27].

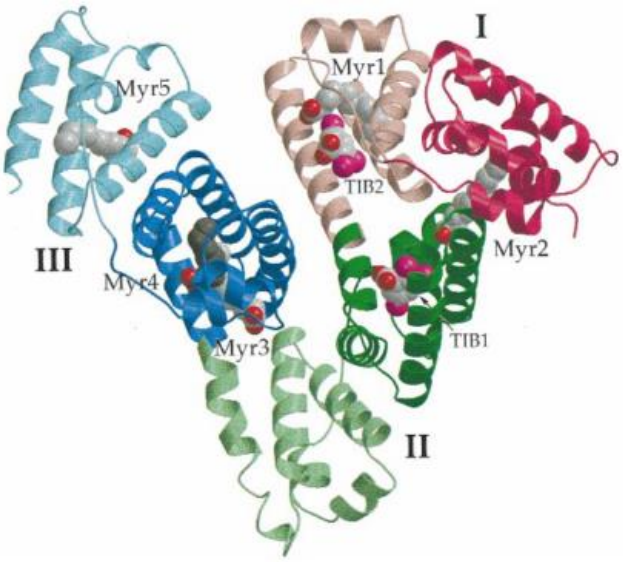

Fig. 1.4.1 The heart-shaped albumin molecule structure [23]

1.4.2 Role of Albumin Agglomerates in Lubrication and Wear Protection:

As mentioned in Section 1.1, a recent study from our group shows that, when subjected to shear, SA alone is able to replicate the shear-mediated transformation of SF, namely the formation of dense aggregates associated with film thickening and increased separation between sheared surfaces [2]. However, the shear conditions for formation of these aggregates, their lifetime, and their exact role in lubrication and wear are still unclear.

Many studies have been done to investigate aggregation phenomena in multi-components fluids when sheared across a large range of synthetic (stiff and nonporous) or natural (compliant and porous) surfaces [3][4][5][14][27][28][29][30][31]. Bin Yang *et. al.* reported in their studies that SA plays a vital role in boundary lubrication by being present as an interfacial layer between shearing surfaces [26]. Aggregation of proteins has been linked with the rheopectic behaviour of SF and SA [4][27], and has been suggested to play a vital role in the rheological and tribological properties of SF [4]. Indeed, Oates *et. al.* reported that protein aggregation was responsible for increasing the viscosity of SF [4]. These aggregates are at times referred to as a "gel phase", *lamina splendens*, or "gel film" by authors, and they have been thought to contribute to the boundary lubrication of SF [26]. Additionally, in their study of CoCrMo prosthetic surfaces sheared against glass in SF, Myant *et. al.* reported that the gel-like film formed at the interface resulting from the aggregation of protein constituents of SF was also responsible for minimising wear of the surfaces [28][29].

Investigating other prosthetic materials such as UHMWPE and 316L stainless steel, Suwandi *et. al.* confirmed that both adhesion between surfaces and presence of wear debris depended on the amount of bovine SA adsorbed onto the sheared surfaces [5]. However, the amount of adsorption varied based on the type of material and its respective hydrophobicity. Similar prostheses were used by H. Mishina *et. al.* in their study using human SA. They found that human SA was able to perform as a boundary lubricant, even upon denaturation [6]. It was reported that SA absorption is significantly higher onto hydrophobic materials than onto hydrophilic ones [5][6][26][32]. The affinity of SA towards hydrophobic surfaces also seems to dictate the amount of wear generated during shear. When diamond-like carbon coatings were sheared across human SA solutions, Hang *et. al.* observed that the wear rate of surfaces was far less than when sheared across simulated body fluid or ambient air [33]. However, the authors did not observe any denaturation of human SA on the opposing surfaces and concluded that this observation was a result of a good boundary lubricating ability of human SA.

1.5 Specific Goals of this Thesis:

Although it was observed that shearing at low speeds usually results in a thicker and more viscous gel-film with better surface adsorption [4][27][29], the range of shearing parameters responsible for the formation of aggregates in SA films is still elusive. Additionally, while it is believed that SA aggregation is intimately related with molecular denaturation – thermally and/or mechanically induced [6][33], the stability (lifetime) and mobility of aggregates has not yet been established, neither their precise role in lubrication and wear. In this thesis, we used the Surface Forces Apparatus (SFA) to investigate in detail the tribological behaviour of SA films when confined and sheared between model mica surfaces. Our research focused on studying (i) the dynamics of formation of aggregates and their stability over time and (ii) the correlation between these aggregates and the resulting friction and wear resistance of the sheared surfaces. As detailed in Chapter II, the SFA allows us to measure friction forces simultaneously to monitoring in situ and in real time the structural transformation of thin films when subjected to a large range of shearing parameters (varied applied load, varied shearing velocity, varied shearing amplitude, varied shearing frequency, varied SA linkage to opposing surfaces, etc.), which helped us to identify the key parameters causing aggregates formation and to discuss the potential mechanisms responsible for shear-induced aggregation in protein films.

1.6 References:

[1] M. K. Kosinska, T. E. Ludwig, G. Liebisch, R. Zhang, H. C. Siebert, J. Wilhelm, U. Kaesser, R. B. Dettmeyer, H. Klein, B. Ishaque, M. Rickert, G. Schmitz, T. A. Schmidt, and J. Steinmeyer, "Articular joint lubricants during osteoarthritis and rheumatoid arthritis display altered levels and molecular species," *PLoS One*, vol. 10, no. 5, pp. 1–18, 2015.

[2] S. G. Cook, Y. Guan, N. J. Pacifici, C. N. Brown, E. Czacko, M. S. Samak, L. J. Bonassar, and D. Gourdon "Dynamics of Synovial Fluid Aggregation under Shear," in revision at *Langmuir* (Special issue Intermolecular Forces and Interfacial Science), 2019.

[3] X. Banquy, D. W. Lee, S. Das, J. Hogan, and J. N. Israelachvili, "Shear-induced aggregation of mammalian synovial fluid components under boundary lubrication conditions," *Adv. Funct. Mater.*, vol. 24, no. 21, pp. 3152–3161, 2014.

[4] K. M. . Oates, W. E. Krause, R. L. Jones, and R. H. Colby, "Rheopexy of synovial fluid and protein aggregation," *J. R. Soc. Interface*, vol. 3, no. 6, pp. 167–174, 2006.

[5] J. S. Suwandi, R. E. M. Toes, T. Nikolic, and B. O. Roep, "Adsorption of albumin on prosthetic materials: Implication for tribological behavior," *Clin. Exp. Rheumatol.*, vol. 33, pp. 97–103, 2015.

[6] H. Mishina and M. Kojima, "Changes in human serum albumin on arthroplasty frictional surfaces," *Wear*, vol. 265, no. 5–6, pp. 655–663, 2008.

[7] R. C. Andresen Eguiluz, S. G. Cook, C. N. Brown, F. Wu, N. J. Pacifici, L. J. Bonassar, and D. Gourdon, "Fibronectin mediates enhanced wear protection of lubricin during shear," *Biomacromolecules*, vol. 16, no. 9, pp. 2884–2894, 2015.

[8] A. J. Sophia Fox, A. Bedi, and S. A. Rodeo, "The basic science of articular cartilage: Structure, composition, and function," *Sports Health*, vol. 1, no. 6, pp. 461–468, 2009.

[9] S. Jahn and J. Klein, "Lubrication of articular cartilage," *Phys. Today*, vol. 71, no. 4, pp. 48–54, 2018.

[10] A. Y. Hui, W. J. McCarty, K. Masuda, G. S. Firestein, and R. L. Sah, "A systems biology approach to synovial joint lubrication in health, injury, and disease," *Wiley Interdiscip. Rev. Syst. Biol. Med.*, vol. 4, no. 1, pp. 15–37, 2012.

[11] T. Bennike, U. Ayturk, C. M. Haslauer, J. W. Froehlich, B. L. Proffen, O. Barnaby, S. Birkelund, M. M. Murray, M. L. Warman, A. Stensballe, and H. Steen, "A normative study of the synovial fluid proteome from healthy porcine knee joints," *J. Proteome Res.*, vol. 13, no. 10, pp. 4377–4387, 2014.

[12] T. A. Schmidt, N. S. Gastelum, Q. T. Nguyen, B. L. Schumacher, and R. L. Sah, "Boundary lubrication of articular cartilage: Role of synovial fluid constituents," *Arthritis Rheum.*, vol. 56, no. 3, pp. 882–891, 2007.

[13] S. M. McNary, K. A. Athanasiou, and A. H. Reddi, "Engineering Lubrication in Articular Cartilage," *Tissue Eng. Part B Rev.*, vol. 18, no. 2, pp. 88–100, 2012.

[14] V. Tirtaatmadja, D. V. Boger, and J. R. E. Fraser, "The dynamic and steady shear properties of synovial fluid and of the components making up synovial fluid," *Rheol. Acta*, vol. 23, no. 3, pp. 311–321, 1984.

[15] T. M. Tamer, "Hyaluronan and synovial joint: Function, distribution and healing," *Interdiscip. Toxicol.*, vol. 6, no. 3, pp. 111–125, 2013.

[16] C. P. Neu, K. Komvopoulos, and A. H. Reddi, "The Interface of Functional Biotribology and Regenerative Medicine in Synovial Joints," *Tissue Eng. Part B Rev.*, vol. 14, no. 3, pp. 235–247, 2008.

[17] S. Bowman, M. E. Awad, M. W. Hamrick, M. Hunter, and S. Fulzele, "Recent advances in hyaluronic acid based therapy for osteoarthritis," *Clin. Transl. Med.*, vol. 7, no. 1, p. 6, 2018.

[18] M. Daniel, "Boundary cartilage lubrication: Review of current concepts," *Wiener Medizinische Wochenschrift*, vol. 164, no. 5–6, pp. 88–94, 2014.

[19] G. Musumeci, "Critical review The role of lubricin in normal and pathological joint tissue : a contemporary review," *OA Anatomy.*, vol. 1, no. 1, pp. 1–6.

[20] A. Dedinaite, "Biomimetic lubrication," *Soft Matter*, vol. 8, no. 2, pp. 273–284, 2012.

[21] R. Teshima, T. Otsuka, and N. Takasu, “Structure of the Superficial Layer of Articular Cartilage,” *J Bone Jt. Surg Br.*, vol. 77 (B), no. 3, pp. 460–464, 1995.

[22] D. C. Carter and J. X. Ho, “Structure of Serum Albumin,” *Adv. Protein Chem.*, vol. 45, pp. 153–203, 1994.

[23] S. Curry, H. Mandelkow, P. Brick, and N. Franks, “Crystal structure of human serum albumin complexed with fatty acid reveals an asymmetric distribution of binding sites,” *Nat. Struct. Biol.*, vol. 5, no. 9, pp. 827–835, 1998.

[24] R. Crockett, “Biochemical composition of the superficial layer of articular cartilage,” *J. Biomed. Mater. Res.*, vol. 82, no. 1, pp. 958–964, 2017.

[25] X. M. He and D. C. Carter, “Atomic structure and chemistry of human serum albumin.,” *Nature*, vol. 358, no. 6383, pp. 209–215, 1992.

[26] C. Bin Yang, H. W. Fang, H. L. Liu, C. H. Chang, M. C. Hsieh, W. M. Lee, and H. T. Huang, “Frictional characteristics of the tribological unfolding albumin for polyethylene and cartilage,” *Chem. Phys. Lett.*, vol. 431, no. 4–6, pp. 380–384, 2006.

[27] J. Fan, C. W. Myant, R. Underwood, P. M. Cann, and A. Hart, “Inlet protein aggregation: A new mechanism for lubricating film formation with model synovial fluids,” *Proc. Inst. Mech. Eng. Part H J. Eng. Med.*, vol. 225, no. 7, pp. 696–709, 2011.

[28] C. W. Myant and P. Cann, “The effect of transient conditions on synovial fluid protein aggregation lubrication,” *J. Mech. Behav. Biomed. Mater.*, vol. 34, pp. 349–357, 2014.

[29] C. Myant, R. Underwood, J. Fan, and P. M. Cann, “Lubrication of metal-on-metal hip joints: The effect of protein content and load on film formation and wear,” *J. Mech. Behav. Biomed. Mater.*, vol. 6, pp. 30–40, 2012.

[30] J. Fan, C. Myant, R. Underwood, and P. Cann, “Synovial fluid lubrication of artificial joints: Protein film formation and composition,” *Faraday Discuss.*, vol. 156, pp. 69–85, 2012.

[31] C. Myant and P. Cann, “On the matter of synovial fluid lubrication: Implications for Metal-on-Metal hip tribology,” *J. Mech. Behav. Biomed. Mater.*, vol. 34, pp. 338–348, 2014.

[32] S. Karimi, T. Nickchi, and A. Alfantazi, “Effects of bovine serum albumin on the corrosion behaviour of AISI 316L, Co-28Cr-6Mo, and Ti-6Al-4V alloys in phosphate buffered saline solutions,” *Corros. Sci.*, vol. 53, no. 10, pp. 3262–3272, 2011.

[33] R. Hang and Y. Qi, “A study of biotribological behavior of DLC coatings and its influence to human serum albumin,” *Diam. Relat. Mater.*, vol. 19, no. 1, pp. 62–66, 2010.

[34] S. L. Bevill, A. Thambyah, and N. D. Broom, “New insights into the role of the superficial tangential zone in influencing the microstructural response of articular cartilage to compression,” *Osteoarthr. Cartil.*, vol. 18, no. 10, pp. 1310–1318, 2010.

Chapter - II : Methodology and Sample Preparation

2.1 Tribology at the nanoscale:

2.1.1 What is tribology?

Tribology, i.e., the study of friction, lubrication, and wear is important in understanding the atomic processes that occur at the interface of two materials when brought and sheared together, as it provides an insight into many technological problems. When two surfaces are in contact, the interfacial interactions involve static and dynamic forces. Unlike pressure, frictional forces are distributed over the interacting contact points, and are not concentrated on a single point or over the entire volume. Friction is a force that is linearly proportional to the number of atoms interacting chemically with each other over the contact [1]. Because realistic surfaces are often rough and exhibit heterogeneous chemical composition, friction is always present at interfaces.

Friction is a result of the interaction between asperities present on the contact area of two sliding surfaces. Asperities are nothing but smaller contact areas occurring purely due to the roughness of the surface. The well-known Amonton's laws state that frictional force F_{fr} occurring between two interacting macroscopic surfaces is linearly proportional to the applied load L:

$$F_{fr} = \bar{\mu} L,$$

where $\bar{\mu}$ is the macroscopic coefficient of friction. Not only does F_{fr} linearly depend on L, but at the macroscopic level it is also independent of the total contact area $A_{contact}$. Interestingly, it was reported that this linearity observed between the frictional force and the applied load at the macroscopic level stays valid at the nanoscale when adhesion between the contacting surfaces is negligible[1]. As contact only occurs at the asperities [2], it was studied that the total area of these interacting asperities $\sum A_{asp}$, also called *real* area of contact, is orders of magnitude smaller than the *apparent* area of contact $A_{contact}$ [1]. Bowden and Tabor formulated the following expression

$$F_{fr} = \tau \sum A_{asp},$$

where, τ is the effective shear strength of the interacting bodies. Various models were later developed based on the single asperity theory to quantify F_{fr} that could be described by existing continuum mechanics theories. This recognised the importance of studying a single

asperity contact for characterising surface roughness and in-turn understanding the tribological properties of multi-asperities realistic surfaces. These single asperities, having radii of curvature ranging from a few nanometres to micrometres, led to the development of various force scanning and computational tools aimed at providing the fundamental understanding of interactions occurring between contact surfaces at the nanoscale. This consequently paved way to the emergence of a new filed of nanotribology.

The characteristics of interfacial interactions taking place between two surfaces when brought together, sheared past each other, or when they are separated after being in contact, have long being studied experimentally at the nanoscale. These studies have led to a conscious understanding of how the normal forces acting between the surfaces differ considerably when there exists a thin film of liquid or polymer between them [2]. A better understanding of these frictional properties has provided an insight into the behavioural nature of lubricants at the molecular level, which often otherwise cannot be understood on the basis of their behaviour at the macroscopic level. This understanding holds crucial for inventing technological solutions for lubrication problems spread across humans to machines.

Hertz was first to develop a model for non-adhesive contact between homogenous and linearly elastic spheres, who showcased that friction is not proportional to the external load but rather $F_{fr} \propto L^{2/3}$ since $F_{fr} = \tau * A_{asp}$ (where τ is the so-called shear strength) and $A_{asp} \propto L^{2/3}$ (See Table 2.1.1). The Maugis-Dugdale model included adhesion effects and showed that friction and A_{asp}, both are a sublinear function of L. Yifei Mo *et al.* from their studies concluded that at the nanoscale frictional force is in fact proportional to the contact area $F_{fr} \propto A_{contact}$ contrary to being proportional to A_{asp} observed at the macroscale [1]. However, they stated that the relationship between F_{fr} and L at macroscale could be extended to the nanoscale too for non-adhesive and adhesive contacts (See Table 2.1.1). In all SA studies presented in this thesis, we followed Amonton's law to extract the coefficients of friction from the friction forces reported, as all the normal forces we measured on SA films (prior and during each shear characterization) confirmed that all forces involved were exclusively repulsive (no adhesive component) and that friction exhibited a linear dependency on normal applied load.

Table 2.1.1 Shows different models explaining the relationship between frictional force, area, and applied load at macroscopic level.

Model	**F_{fr} vs Area**	**F_{fr} vs Load**
Multi-Asperity		
• **Amonton's Laws** • **Bowden and tabor**	Independent of contact area $F_{fr} = \tau \sum A_{asp}$	$F_{fr} = \bar{\mu} L$ $F_{fr} = \bar{\mu} L$
Single-Asperity		
• **Hertz model (Non-adhesive contact)** • **Maugis-Dugdale model (Adhesive contact)**	$F_{fr} = \tau * A_{asp}$ $F_{fr} = \tau * A_{asp}$	$F_{fr} \propto L^{2/3}$ F_{fr} sublinear function of L

2.1.2 The Surface Forces Apparatus (SFA): A Tool for Nanotribology:

The Surface Forces Apparatus (SFA) was developed by Jacob Israelachvili in the early 1970s, when he was a PhD student at the Cavendish Laboratory of Cambridge University (UK) under the supervision of David Tabor. The SFA Mark III (SurForce, Santa Barbara CA) was used to carry out all the experiments in our study. The SFA can be used to study the properties of a lubricant by characterising its adhesion to surfaces, its friction, and its ability to protect surfaces from wear. An ideal lubricant should (i) adhere to the surface (so it is not expelled from the junction when surfaces are sheared), (ii) have a stable low coefficient of friction, and (iii) ensure wear protection of surfaces. Lubrication, in scenarios where smooth motion is necessary, minimises the adhesion between two surfaces and protects them from damage. SFA is used to understand the nature of forces between two surfaces across a thin film of lubricant (liquid or solid), as it gives an insight into whether these surfaces, when pressed together, exhibit adhesive or repulsive forces, which is desirable as it indicates that both surfaces are still separated by a thin lubricant layer. To understand this behaviour at the interfacial level is of paramount importance because if two surfaces are sheared together, either high friction or film depletion often leads to surface damage. However, experiments have shown that when there exists one or more molecular layers of liquid acting as a lubricating film during the sliding movement, it drastically reduces the coefficient of friction, in-turn reducing the value of F_{fr}

and ensuring smooth sliding, thereby protecting the surfaces [2]. Therefore, studying the tribological properties of thin films at the molecular level holds key to developing efficient lubricants.

SFA uses interferometric Newton rings to observe the contact junction between the surfaces prior, during and after shear. Briefly, two silica discs covered with back silvered-mica atomically smooth sheets and placed in a cross-axial configuration form the two opposing surfaces between which the thin lubricant film is confined. White light is passed through these discs where it gets reflected back and forth by the silver layer, and this forms an optical interferometer allowing for multiple beam interferometric measurements. The cross-axial configuration acts as a plano-convex setup, enabling us to observe Newton's Rings caused by the constructive and destructive interferences generated (Fig. 2.1.1). The outgoing beam from these surfaces is then directed onto a grating spectrometer, which is further connected to a CCD camera. This transmitted light consists of discrete wavelengths that are observed as fringes. These fringes of equal chromatic order (FECO), further explained in Section 2.2, are then monitored in real time to study the film characteristics (thickness, refractive index, presence of aggregates etc.) prior and during shearing. The general optical setup is described in fig 2.1.2.

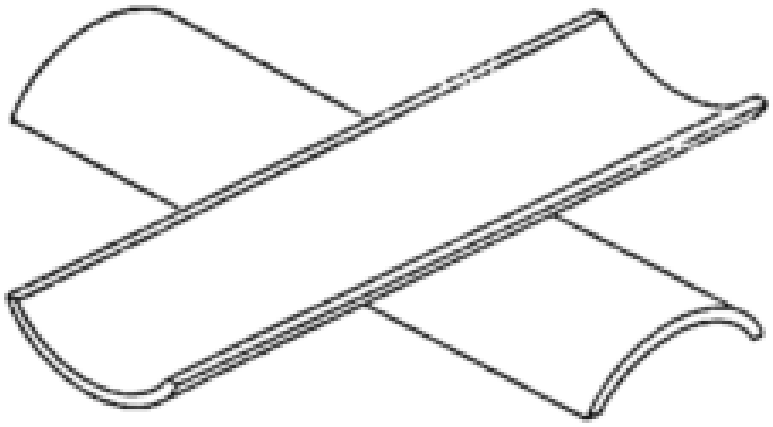

Fig. 2.1.1 Cross-axial configuration of silica discs

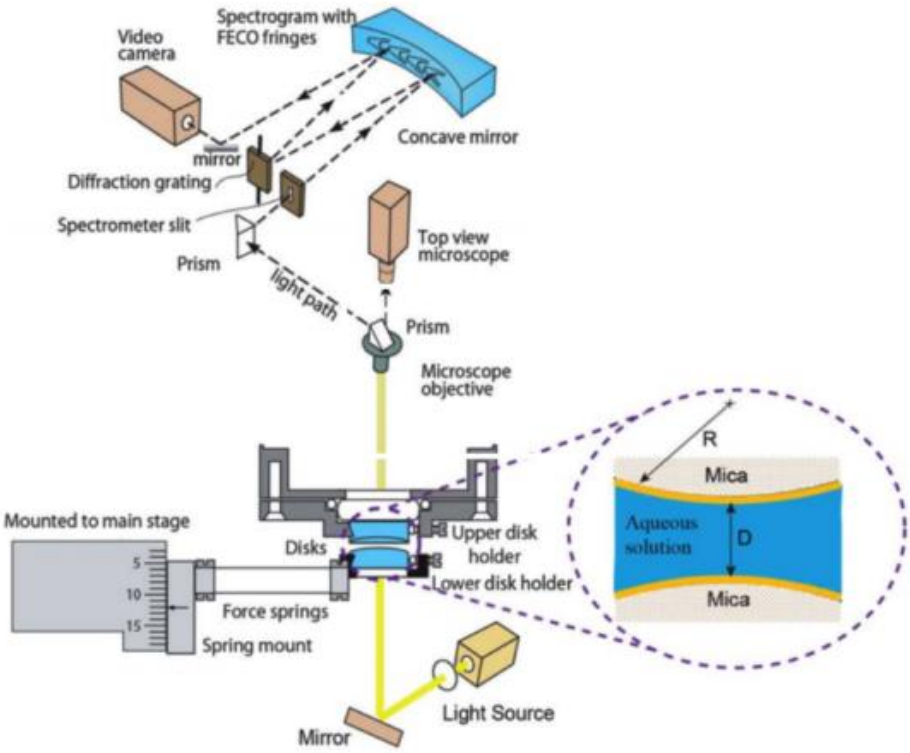

Fig. 2.1.2 Optical setup of SFA

Apart from the SFA, various tools such as the Atomic Force Microscopy (AFM) or the pin-on-disk tribometer have been used extensively in the field of nano and micro-tribology. Just like the AFM that uses deflection of a cantilever to apply/measure forces via laser deflection, the SFA uses the same principle where the deflection is measured using strain gauges. While the AFM is used to study the surface properties of nano-asperities using a nanotip without control over real applied stress nor asperities thickness because the contact area can only be estimated based on tip dimensions, the SFA is used to study bigger asperities (typically micron scale) with a high control over stress, contact area, film thickness and damage at the interface due to the use of FECO fringe interferometry simultaneously to force measurements.

2.1.3 Mica Surface Preparation for SFA Measurements:

All preliminary surfaces in SFA measurements are made of mica. Mica sheets (S&J Trading, Glen Oaks, NY) free from steps were used to prepare surfaces. A large and thick mica piece ($0.5mm - 1\ \mu m$) was first cleaved, which served as a backing/protecting sheet for the cleaved mica pieces used as later as substrates. For the substrate pieces, mica was cleaved multiple times to get very thin pieces ($2\mu m - 4\ \mu m$), which were placed on the backing sheet, clean side down. Care was taken that each piece was large enough to cover the area of two

silica discs. The homogeneity of these pieces (absence of steps) was determined from their uniform colour under grazing incident light. Before placing these pieces onto the backing sheet, their edges were cured using a hot platinum wire (0.2 mm) that was connected to a low voltage DC power supply. This was done to reduce the surface energy of the edges in order to make it possible for the pieces to be peeled off the backing sheet after silvering.

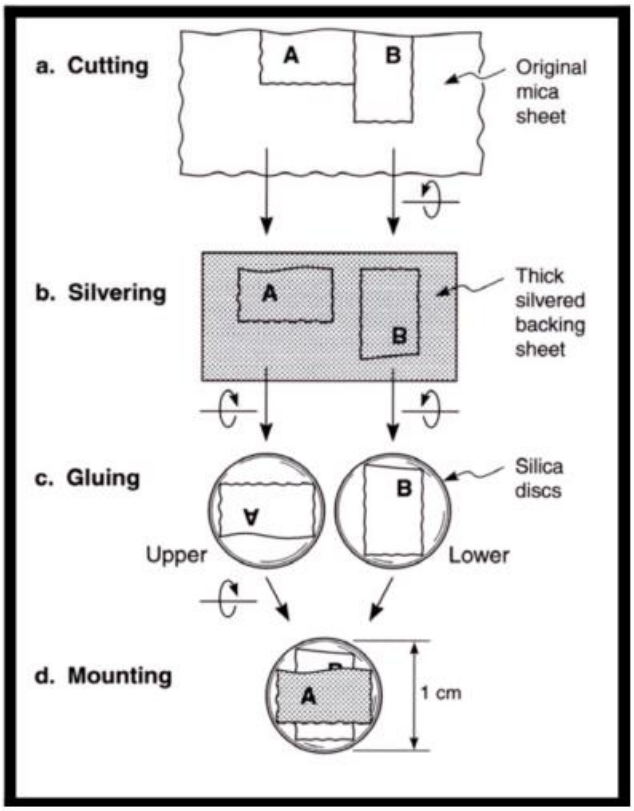

Fig. 2.1.3 General procedure for surface preparation

This backing sheet was then silvered using an e-beam evaporator (ANGSTROM NEXDEP) in a clean room, in a vacuum chamber of about 2.5 x 10-7 Torr, at a deposition rate of $0.5\ \text{Å}/s$. The resulting average silver layer thickness was set between 50 – 55nm for optimal interferometric measurements. These silvered mica pieces were then glued onto the silica discs with radius of curvature of $1cm$ using optical UV-curing glue (Norland, Cranbury, NJ), which was then left under UV light for 2 hours for curing. All steps were performed in a laminar flow hood ensuring minimum number of particles and contamination. Fig. 2.1.3 explains the general procedure of mica surfaces preparation.

2.1.4 Lubricant Solution Preparation and Incubation:

Human plasma fibronectin (FN) (Sigma Aldrich, St. Louis MO) was diluted to $0.02mg/ml$ in phosphate buffer saline (PBS). Bovine serum albumin (BSA) (powder form)

(Sigma Aldrich, St. Louis MO) was diluted in PBS to reach a concentration of $8mg/ml$. Both these solutions were prepared with sterile PBS of 1X strength. Before incubation, each solution was centrifuged for five minutes at 12RPM to avoid the presence of any protein aggregates prior to shear. Additionally, BSA was kept in the SFA experimental room prior to usage to reach thermal equilibrium faster after incubation. This was done because the temperature of the SFA room (≈ 28°C) was systematically higher than that of the main lab temperature.

The freshly prepared back-silvered mica surfaces were mounted in the SFA and separated by several millimeters. 50 µL of soluble FN was injected between the surfaces to form a meniscus and coat both opposing mica surfaces. The FN was incubated for 30 minutes to allow appropriate adsorption onto the mica surfaces, and then rinsed with PBS. A 55 µL droplet of dilute BSA was then incubated between the FN-coated surfaces for 1 hour and was left in the junction after incubation to be used as shearing medium.

Preparation of solutions and incubation were carried out in a laminar flow hood to keep both surfaces and SFA chamber free of contamination at all times.

2.2 Data Acquisition and Analysis:

The SFA has the unique ability of measuring normal (adhesion) and lateral (friction) forces via double spring deflection technique while simultaneously monitoring film thickness, size and shape of the shearing junction, distribution and index of refraction of aggregates (if any), and presence of surface damage via the FECO Fringe Interferometry technique. LightField (Princeton Instruments, Trenton NJ) was used to view and acquire interferometric (FECO) data while LabView (National Instruments, Austin TX) was used for acquiring friction data. Analysis of data was done using MATLAB (MathWorks, Natick MA) and Microsoft Excel.

2.2.1 Film Thickness Measurements via FECO Fringes Interferometry:

Let us consider two semi reflective back-silvered mica surfaces in contact, when white light is directed through this silvered “sandwich”, multiple interferences occur between the surfaces. The emerging transmitted beam of light is then sent in the slit of a grating spectrometer, which splits up the wavelengths that are seen as an ordered collection of fringes. These fringes are called ‘Fringes of Equal Chromatic Order’ or FECO, and these wavelengths are discrete with value λ_n^0, where n = 1,2,3, and so on (n is called the fringe order). Using these FECO, the SFA can measure film thickness down to a few Å [3][4].

When two mica sheets of identical thickness are separated by a distance D, the whole FECO pattern shifts to longer wavelengths λ_n^D with respect to their (mica-mica contact) position λ_n^0. The distance D between these surfaces is determined by measuring the shifts in the wavelengths of odd and even ordered fringes.

D can be calculated using the following formula:

$$\tan\left(2\pi\mu\frac{D}{\lambda_n^D}\right) = \frac{2\bar{\mu}sin\left[\frac{1-\lambda_n^0/\lambda_n^D}{1-\lambda_n^0/\lambda_{n-1}^0}\pi\right]}{(1+\bar{\mu})\cos\left[\frac{1-\frac{\lambda_n^0}{\lambda_n^D}}{1-\frac{\lambda_n^0}{\lambda_{n-1}^0}}\pi\right] \pm (\bar{\mu}^2-1)}$$

where

$\lambda_n^D = Wavelength\ of\ the\ n\ odd\ fringe\ at\ distance\ D$

$\lambda_n^0 = Wavelength\ of\ n\ odd\ fringe\ at\ D = 0$

$\lambda_{n-1}^0 = wavelength\ of\ the\ even\ fringe\ (n-1)\ at\ D = 0$

$\mu_{mica} = refractive\ index\ of\ mica\ at\ \lambda_n^D$

$\bar{\mu} = \frac{\mu_{mica}}{\mu}$,

$where\ \mu\ is\ the\ refractive\ index\ of\ the\ medium\ between\ the\ two\ mica\ surfaces\ at\ \lambda_n^D$

The + refers to an odd ordered fringe while – refers to the even ordered fringe.

For surface separations D < 300Å, the above equation gets simplified to the following [3]:

$$D = \frac{nFn(\lambda_n^D - \lambda_n^0)}{2\mu_{mica}} \qquad for\ an\ n-odd\ fringe\ (1)$$

While,

$$D = \frac{nFn(\lambda_n^D - \lambda_n^0)\mu_{mica}}{2\mu^2} \qquad for\ n-1\ even\ fringe$$

Here, the factor Fn can be considered to be a correction factor [4] and is calculated using the following formula

$$nFn = \frac{\lambda_{n-1}^0}{\lambda_{n-1}^0 - \lambda_n^0} \quad [4]$$

By nature, mica is birefringent, which means that every fringe appears to be a doublet made of two components γ and β, having their distinct refractive indices μ_γ and μ_β respectively. From these components the value of μ_{mica} can be calculated as follows

$$\mu_{mica} = 1.5820 + \frac{(4.76 * 10^5)}{\lambda^2(\text{Å})}$$

where λ is the mean of $\lambda_\gamma(\text{Å})$ and $\lambda_\beta(\text{Å})$, which are the wavelengths of γ and β components respectively.

Figure 2.2.1 gives an example of the SFA equivalent geometry of two back-silvered mica surfaces in contact, i.e., when $D = 0$ (top) and when separated by a distance $D = 100\text{Å}$ (bottom), accompanied by their corresponding FECO pattern, as seen directly from the eyepiece of a spectrometer (no CCD used). Note that even and odd FECO have different shapes. The even-ordered fringes are wide and curvy; because they have a maximum of electric field at the center of the junction, they are very sensitive to the optical properties of the medium confined between the surfaces and therefore are used for monitoring film aggregation and calculating index of refraction. Instead, odd-ordered fringes are thin and pointy; because they have a minimum of electric field at the center of the junction, they are insensitive to optical properties and are used to make extremely precise film thickness measurements with sub-nanometer resolution.

Figure 2.2.2 shows the FECO acquired through our CCD when the mica surfaces are in contact in air (D = 0), while figure 2.2.3 shows the FECO when the surfaces are separated by a thin film, i.e. when the distance D between opposing surfaces corresponds to the film thickness. (here $D \approx 10nm$). At any time, the wavelength shift $\Delta\lambda_n = \lambda_n^D - \lambda_n^0$ of the n-odd fringe, which corresponds to the difference between the "position" of the n-odd fringe when a film of thickness D is present with respect to its position at D = 0 (when no film is present) allows us to determine accurately the film thickness as follows.

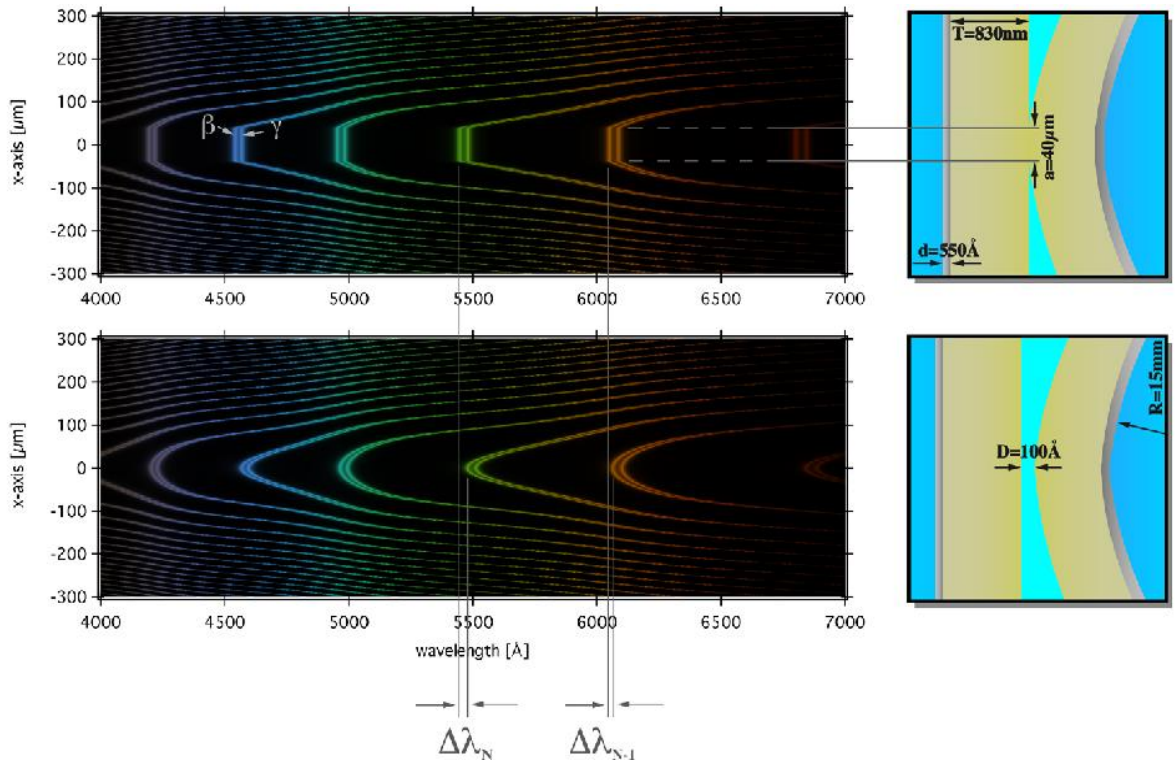

Fig. 2.2.1 Multiple beam interferometry in SFA. Top half denotes the point of closest approach of mica surfaces, the shape, and position of the fringes at D=0. The bottom half denotes the same when a thin film is present between the two surfaces at distance D. $\Delta\lambda_n$and $\Delta\lambda_{n-1}$ are the wavelength shifts for λ_n and λ_{n-1} respectively from which surfaces separation, i.e., film thickness, is calculated [3].

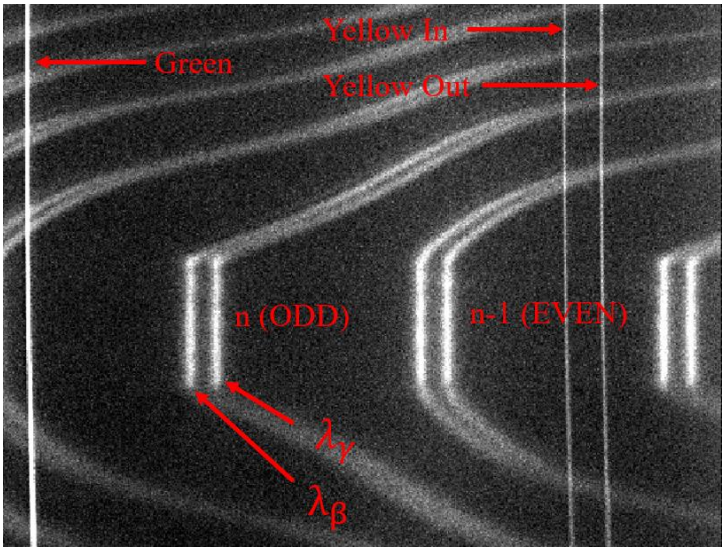

Fig. 2.2.2 FECO pattern of our mica-mica contact in air (D=0), superimposed with Green, Yellow In and Yellow Out Mercury lines used as references to quantify spectrometer dispersion

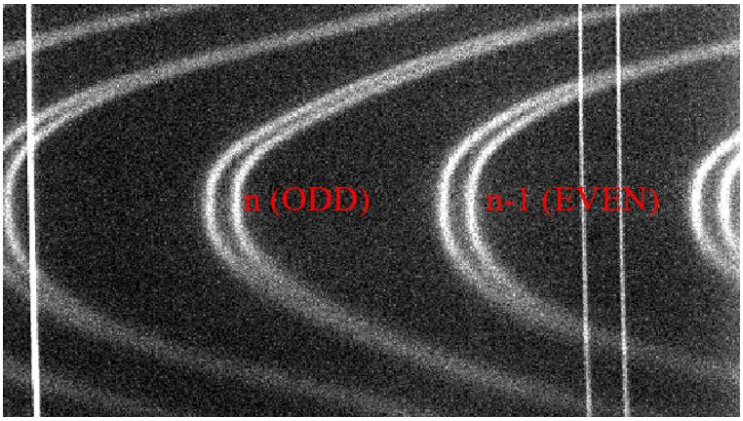

Fig. 2.2.3 Same FECO pattern after introducing a thin film of thickness D between the mica surfaces

As we used a grating spectrometer, we first determined the spectrometer dispersion by using a Mercury lamp with well-defined and visible lines of known wavelengths. Mercury green and yellow lines are also used as reference wavelengths to determine the wavelengths of the fringes n – odd and n-1 – even. Without reference wavelengths it would be impossible to find out λ_n and λ_{n-1} when using a spectrometer and a CCD camera. The reference is used in the following manner:

The position of the green and yellow lines with respect to pixel distance, laterally, is first calculated using LightField (keeping the left edge of the CCD screen as the reference i.e. 0^{th} point). Multiple readings are taken, and finally the mean of these readings is considered for further calculations. Let this distance be X. The wavelengths of the green, yellow-in, and yellow-out lines are already known, which are:

$$\lambda_{Green} = 5460.75 \text{ Å}$$

$$\lambda_{Yellow-in} = 5769.59 \text{ Å}$$

$$\lambda_{Yellow-out} = 5790.654 \text{ Å}$$

We use these to calculate the dispersion (DP) (or in other words Å/pixel) of the spectrometer used for the experiment,

$$\boldsymbol{DP} = \frac{\left(\lambda_{yellow-in} - \lambda_{Green} \Big/ X_{yellow-in} - X_{Green}\right) + \left(\lambda_{yellow-out} - \lambda_{Green} \Big/ X_{yellow-out} - X_{Green}\right)}{2}$$

The above approximation is highly dependent on the pixel distance found from the software used, which when inaccurate can lead to flawed results. For example, if X_{Green} is

measured at 24 (pixel distance) while it is actually 19, this will overestimate the value of λ_{Green}, which will directly affect the value of DP, and hence affecting the final results.

We are exclusively analyzing the FECO located in the green - yellow spectral region because our experimental setup (silica, mica, silver, spectrometer, CCD) have their minimum of absorbance in such region and because most protein films tested in our experiments are transparent at those wavelengths. However, if absorbing films were investigated, the spectrometer we used would be cranked up or down to non-absorbing regions and other Mercury lines (e.g., red or blue) would be used as references.

Now to calculate the wavelength of the n – odd fringe at D = 0, $\lambda_n^0(\text{Å})$, the mean of the pixel distances of both γ and β components are used as follows:

For calculating $\lambda_\beta(\text{Å})$,

$$\lambda_\beta(\text{Å}) = \left[\left(X_{\beta\_\text{mean}} - X_{Green}\right) * DP\right] + \lambda_{Green}$$

Similarly,

$$\lambda_\gamma(\text{Å}) = \left[\left(X_{\gamma\_\text{mean}} - X_{Green}\right) * DP\right] + \lambda_{Green}$$

Finally,

$$\lambda_n^0(\text{Å}) = mean(\lambda_\beta, \lambda_\gamma)$$

Where,

$X_{\beta\_\text{mean}} = mean\ of\ all\ the\ pixel\ readings\ taken\ for\ the\ \beta\ component$

$X_{\gamma\_\text{mean}} = mean\ of\ all\ the\ pixel\ readings\ taken\ for\ the\ \gamma\ component$

The wavelength of n-1 even fringe is also calculated using the above method

$$\lambda_{n-1}^0(\text{Å}) = mean(\lambda_\beta, \lambda_\gamma),$$

where λ_β and λ_γ are the wavelengths of the components of λ_{n-1}^0.

Let us use the above formulae to confirm the values calculated in the data analysis tables showcased in the following images. These results are from one of the experiments performed.

Table 2.2.1 Pixel readings for green, yellow-in, yellow-out lines, n – odd fringe, and n-1 – even fringe, where n = 83.

				n		**n-1**	
	Green	Yellow In	Yellow Out	β	γ	β	γ
	20	402	429	195	216	297	318
	20	403	430	195	217	296	318
	19	403	429	196	217	296	318
	21	404	431	196	217	296	318
	21	403	429	197	217	297	318
Average	20.2	403	429.6	195.8	216.8	296.4	318

Table 2.2.2 Wavelengths of green and yellow lines, the average dispersion value of mica, and the wavelengths of n- odd and n-1 even fringes.

Mercury Line	**Green**	**Yellow In**	**Yellow Out**
λ (Å)	5460.75	5769.59	5790.654
$\lambda\ (Pixel)$	20.2	403	429.6
Average Dispersion = 0.806308			
$\lambda_n^0(\text{Å})$	5610.804		
$\lambda_{n-1}^0(\text{Å})$	5692.16		

From Table 2.2.1

$X_{Green} = 20.2$

$X_{Yellow-In} = 403$

$X_{Yellow-out} = 429.6$

Now dispersion DP of the spectrometer:

$$\boldsymbol{DP} = \frac{\left(5769.59 - 5460.75/403 - 20.2\right) + \left(5790.654 - 5460.75/429.6 - 20.2\right)}{2}$$

$$\boldsymbol{DP} = 0.806308,$$

which corresponds to the value in the table from table 2.2.2.

Now to calculate the wavelength of n – odd fringe $\lambda_n^0(\text{Å})$, we need to calculate the wavelengths of its two components first.

$$\lambda_\beta(\text{Å}) = [(195.8 - 20.2) * 0.806308] + 5460.75$$

$$\lambda_\beta(\text{Å}) = 5602.337$$

Similarly,

$$\lambda_\gamma(\text{Å}) = 5619.270$$

Finally,

$$\lambda_n^0(\text{Å}) = \frac{5602.337 + 5619.270}{2}$$

$$\lambda_n^0(\text{Å}) = 5610.804$$

Similarly,

$$\lambda_{n-1}^0(\text{Å}) = 5692.16$$

Table 2.2.3 Respective values derived during the experiment

nFn	69.9657
n	67
n (odd)	1
n (even)	-1
$\lambda_n^0(\text{Å})$	5610.804
$\lambda_{n-1}^0(\text{Å})$	5692.16

Now nFn can be calculated as follows:

$$nFn = \frac{5692.16}{5692.16 - 5610.804}$$

$$nFn = 69.9660$$

When using mica for measurements at a wavelength of around 5500 Å, the fringe order n can be calculated as follows

$$n = \frac{nFn - 1}{1.024} \quad [2]$$

$$n = \frac{69.9660 - 1}{1.024}$$

$$n = 67.34$$

Rounding 'n' to the nearest whole digit, $n = 67$

While this method does help in deriving the fringe number, a small error in rounding the digit can lead to wrong assumptions, i.e. mistaking an EVEN fringe for an ODD and vice versa. This in turn can give out wrong calculations for the distance D, i.e., either over estimating or under estimating the film thickness values. Hence, care should be taken while calculating n.

Table 2.2.4 A snippet of the data from the experiment

	time	β_n	γ_n	λ_n^D	$\lambda_n^D - \lambda_n^0$	μ_{mica}	D_n	D_n	F/R
Line	Sec	Pixel	Pixel	Å	Å		Å	*nm*	*mN/m*
312	109.091	486.08	506.02	5844.431475	233.6276	1.595935	5121.11	512.1109587	7.981928

In table 2.2.4, columns from left to right denote:

1. The frame number (Line)
2. Time w.r.t to the frame number
3. Pixel distance of β component of the fringe
4. Pixel distance of γ component of the fringe
5. λ_n^D
6. $\lambda_n^D - \lambda_n^0$
7. μ_{mica}
8. Distance D in Angstrom (Film Thickness D in Angstrom)
9. Distance D in nm (Film Thickness D in Angstrom)

The methodology used earlier to calculate λ_n^0 is applicable for calculating λ_n^D too, from the pixel values of both of its components. Therefore, solving the equation we get,

$$\lambda_n^D = 5844.4314$$

Now to calculate μ_{mica}

$$\mu_{mica} = \mathbf{1.582} + \frac{\mathbf{4.76 * 10^5}}{(\lambda_n^D)^2}$$

$$\mu_{mica} = \mathbf{1.582} + \frac{\mathbf{4.76 * 10^5}}{(\mathbf{5844.4314})^2}$$

$$\mu_{mica} = \mathbf{1.5959}$$

Once λ_n^D and μ_{mica} are known, D_n can be calculated using formula (1) described earlier

$$D_n = \frac{69.9660 * (5844.4314 - 5610.804)}{2 * 1.5959}$$

$$D_n = 5121.110 \text{ Å}$$

$$D_n = 512.11\, nm$$

For every position of the n – odd fringe with λ_n^D at a particular time, D can be calculated as explained above and used further to measure forces between the surfaces at that particular time and position using pixel values and other known reference values mentioned.

2.2.2 Normal Force Measurements:

The SFA lower surface is mounted on a horizontal double cantilever spring. The stiffness of this spring is calibrated before the experiment to get the spring constant $K(^N/_m)$. In our experiments, the value of K was measured to be 1656 $^N/_m$. When normal force is applied on the surfaces, the spring is deflected as a result of the interaction. For attractive forces, the spring is deflected in the upward direction towards the upper surface, while for repulsive forces it is deflected downwards. To measure the forces between the two surfaces Hooke's law is applied using the information from the surface separation distance and the amount of spring deflection.

The displacement of the lower surface is controlled by a step motor, whose speed and linearity are calibrated prior to each experiment using FECO displacement far from contact, i.e., when no force (even long-range forces) act on the surfaces. Let the new position at which the lower surface is moved to be D_0, which also denotes the displacement of the motor. When it is moved towards the upper surface, this will cause the spring to deflect. This deflection is given by $D - D_0$, where D is the distance between the surfaces due to the displacement D_0 [3]. Hence, the force at this new position is given by

$$F = K(D - D_0)$$

When there is attraction between the surfaces, $D < D_0$, and for repulsion $D > D_0$ [3].
Now, to calculate the normal force at every position *vs.* time, distance is first plotted as a function of time, far from contact (where F = 0) to get the speed (and initial position) of the step motor.

Table 2.2.5 shows the Force/Radius value for frame number 331. Distance D_n has already been calculated in section 2.2.1. To get time for the frame number, the FPS (frame/sec) value has already been acquired while recording the data using the CCD camera and the spectrometer. The FPS for the experiment was 2.86. Hence, each frame took 0.34965 seconds. Therefore,

$$for\ frame\ 312, time = 312 * 0.34965\ (\text{sec})$$

$$time = \ 109.091\ (sec)$$

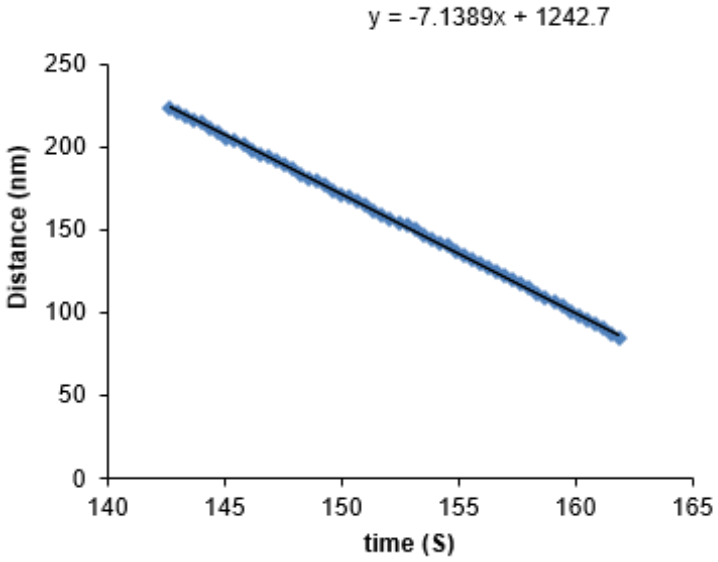

Fig. 2.2.4 The linear regime of the distance vs. time is used to calculate the speed of the step motor used to displace the lower surface. Here are the speed and the 'Y' intercept values for the example experiment discussed in section 2.2.1

Table 2.2.5 Radius of the silica disc R, spring constant K, Slope and intercept of the linear regime

R(cm)	1
K(mN/m)	1656000
Motor Calibration	
Slope	-7.1389
Intercept	1242.7

Now, at $t = 0$, we know that the position of the motor was at 1242.7 nm ('Y' intercept), therefore displacement at $t = 109.091$ will be:

$$Speed\ of\ the\ motor = -7.1389\ nm/sec$$

The negative sign indicates a negative slope of the linear regime.

Hence,

$$displacement_{t=109.091} = (speed * time)$$

$$displacement_{t=109.091} = -778.7897\ nm$$

Now,

$$D_0(total\ displacement) = displacement_{t=109.091} + position\ at\ t = 0$$

$$D_0 = -778.7897 + 1242.7$$

$$D_0 = 463.9103\ nm$$

Since the radius R of the silica discs remains approximately constant throughout our force application (unless high pressures are applied, which was not the case here), the force F could be measured over radius R as follows:

$$F/R = K(D_n - D_0)/R$$

$$F/R = 1656000[512.1109 - (463.9103)]mN/cm$$

$$F/R = 79820193.6\frac{nN}{cm}$$

$$F/R = 7.9820\ mN/m,$$

which corresponds to the value of F/R from table 2.2.4.

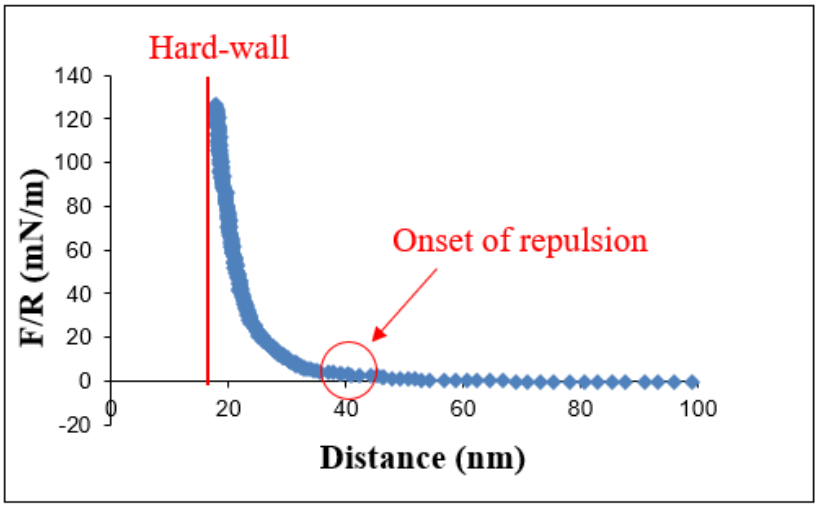

Fig. 2.2.5 Normal force F/R vs. Distance profile of the confined thin film

Using the above methodology, F/R is measured at all the positions and plotted against distance to get the F/R force versus distance response of the thin film, as shown in Fig 2.2.5. The "hard-wall" denotes the thickness of the film under maximum applied load. The onset of interaction is the distance at which opposing surfaces start "feeling" interactive forces, which corresponds to the thickness of undeformed 'equilibrated' films.

2.2.3 Friction Force Measurements:

The horizontal spring that holds the lower surface (mentioned in Section 2.2.2) is itself attached to a bimorph slider that provides lateral displacement, while the upper surface is mounted on a vertical double spring device that detects the resulting friction forces (as detailed below and in Fig. 2.2.6). FECO are used prior and during shearing to monitor the size and shape of the surfaces, the formation of aggregates, and the evolution of film thickness.

The bimorph slider (Fig. 2.2.7) is made of two parallel piezoelectric material ceramic strips configured in opposite polarities. When voltage is applied across the bimorph, one strip expands while the other contracts. A triangular signal is used to achieve a back-and-forth lateral movement, as deformation of each ceramic strip is proportional to the applied voltage (when it is below 100V). In our experiments, input signals of varied amplitudes (5V and 20V) and varied frequencies (0.0125 Hz to 0.2 Hz) were used to achieve various shearing velocities (Fig. 2.2.8).

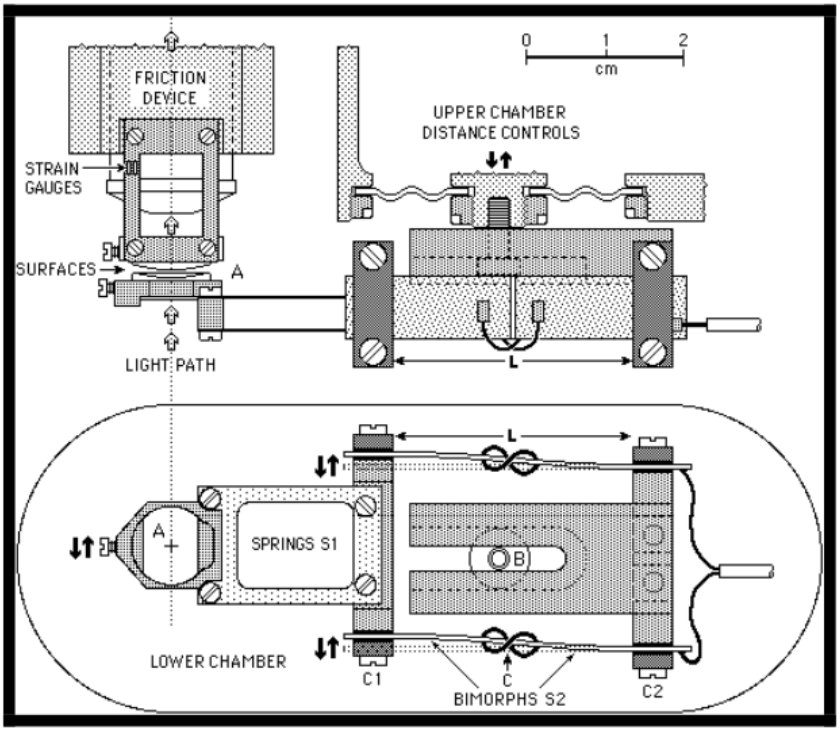

Fig. 2.2.6 Friction device and bimorph slider assembly (side and top views)

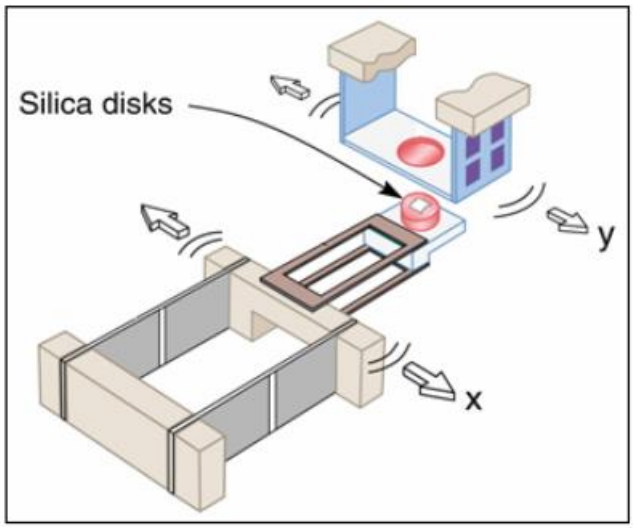

Fig. 2.2.7 Lateral displacement actuation and friction detection

The upper surface is mounted on a so-called friction device, which consists of a vertical double cantilever spring with strain gauges installed on their sides for lateral displacement (friction) detection. The strain gauges output a voltage that is further used to calculate the frictional force. The friction device comes in different sensitivity levels i.e. varied spring stiffness. Depending upon the range of frictional forces that need to be detected, a device with suitable sensitivity level can be used. The device was pre-calibrated before the experiment to

(i) establish the relationship between voltage readout and friction force, (ii) ensure linearity of the friction vs. displacement and (iii) correct the balance between left-to-right and right-to-left displacements.

When surfaces are ‘sliding’ past each other, the output of the friction device are rectangular loops, the upper part (or the positive values of V) denotes the friction between opposing surfaces during left-to right displacements while the lower part (or the negative values of V) denote the friction during right-to-left displacements (Fig. 2.2.9). Overall, the frictional force in V is measured as the average of the two values gathered, and later converted in mN after calibration of our friction device.

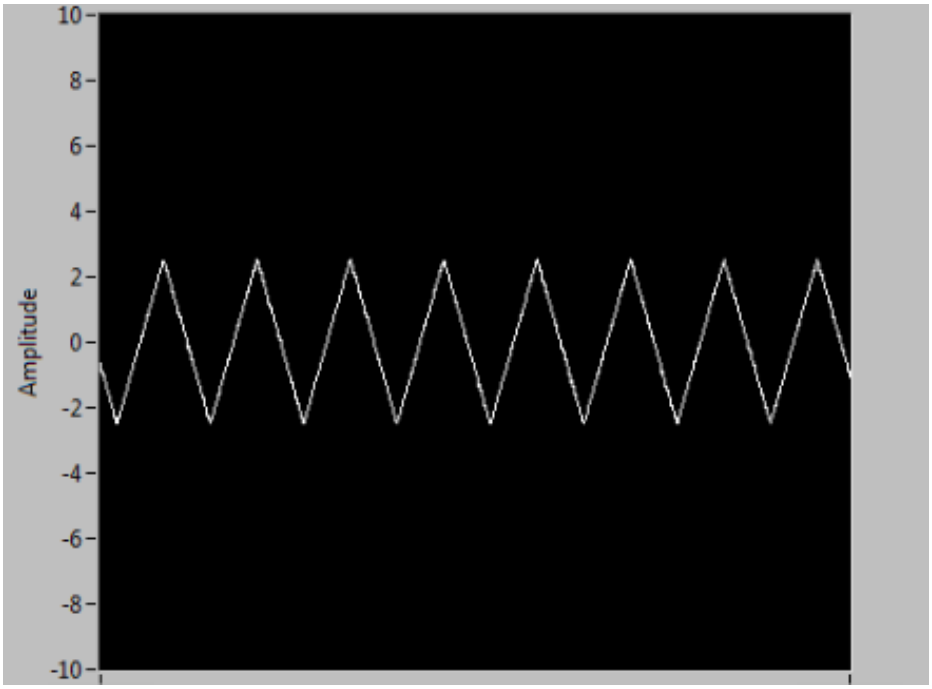

Fig. 2.2.8 Function generator triangular signal is used as input for the bimorph slider, typically here 5V peak-to-peak amplitude at 0.05Hz, as used in many of our experiments

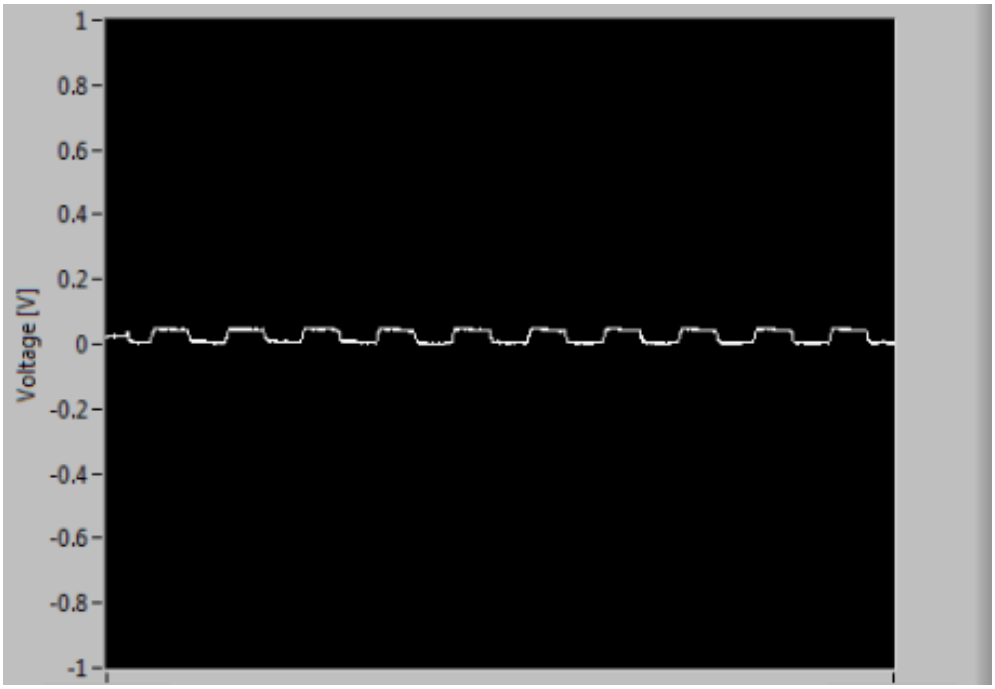

Fig. 2.2.9 Friction output signal (friction loops), as recorded by our friction device

2.3 References

[1] Y. Mo, K. T. Turner, and I. Szlufarska, "Friction laws at the nanoscale," *Nature*, vol. 457, no. 7233, pp. 1116–1119, 2009.

[2] J. N. Israelachvili, B. Bhushan, and U. Landman, "Nanotribology: friction, wear and lubrication at the atmoic scale," *Lubricants*, vol. 1, no. 4. pp. 102–131, 2013.

[3] J. Israelachvili, *USER'S MANUAL for SFA3 and SFA2000 with Attachments*, May. 2009.

[4] J. N. Israelachvili, "Thin film studies using multiple-beam interferometry," *J. Colloid Interface Sci.*, vol. 44, no. 2, pp. 259–272, 1973.

Chapter - III : Results

Our research aimed at elucidating the shear-mediated transformation of SA films. Specifically, we focused on (i) identifying the parameters responsible for the formation of aggregates and (ii) correlating these aggregates with friction and wear resistance of the sheared surfaces. To do so, we quantified film thickness, structural changes and friction forces in SA films while varying the following factors: shear parameters (such as shear velocity, frequency and/or amplitude) in section 3.1, applied load in section 3.2, strength of attachment of SA to surfaces in section 3.3, and previous shear history in section 3.4.

3.1 Effect of Shearing Parameters:

As mentioned in Chapter 1, although some reports indicated that 'low' shearing speeds would produce thicker films, neither the range of speeds tested nor the shear frequency and the amplitude utilised were accurately reported. As summarized in Table 3.1, here we explored four different sets of shearing parameters (called Protocols) in which we varied shearing velocity (*Vshear)*, shearing amplitude, and shearing frequency. Except for protocol 1 (P1), all other protocols were sheared for about an hour and a half while P1 was sheared for about an hour.

Table 3.1.1 Four shearing protocols used for the tests

Protocol	**Shearing Frequency (Hz)**	**Shearing Voltage (V)**	**Seconds per Shearing Cycle (s)**	**Shearing Amplitude (µm)**	**V_{shear} (µm/s)**
P1	0.05	5	20	17.5	0.875
P2	0.0125	20	80	70	0.875
P3	0.05	20	20	70	3.5
P4	0.2	5	5	17.5	3.5

3.1.1 Normal-Force Profile

Prior to each shearing session, a normal-force test was carried out to (i) evaluate the thickness of the SA film adsorbed onto surfaces before compression (a.k.a. uncompressed film thickness), as determined by the onset of repulsion between surfaces (Fig 3.1.1) and (ii) measure the thickness of the film after compression before shearing was started. The applied loads for the normal-force tests were all kept below $2mN$ to avoid load-induced denaturation of SA molecules. The force-distance profile displayed in Fig 3.1.1 indicates an onset of

repulsion at circa 24 nm (corresponding to a 24/2 = 12 nm thick SA film adsorbed onto each mica surface) and a 'hard wall' at circa 9 nm (corresponding to a compressed film thickness of 4.5 nm on each surface before shear started).

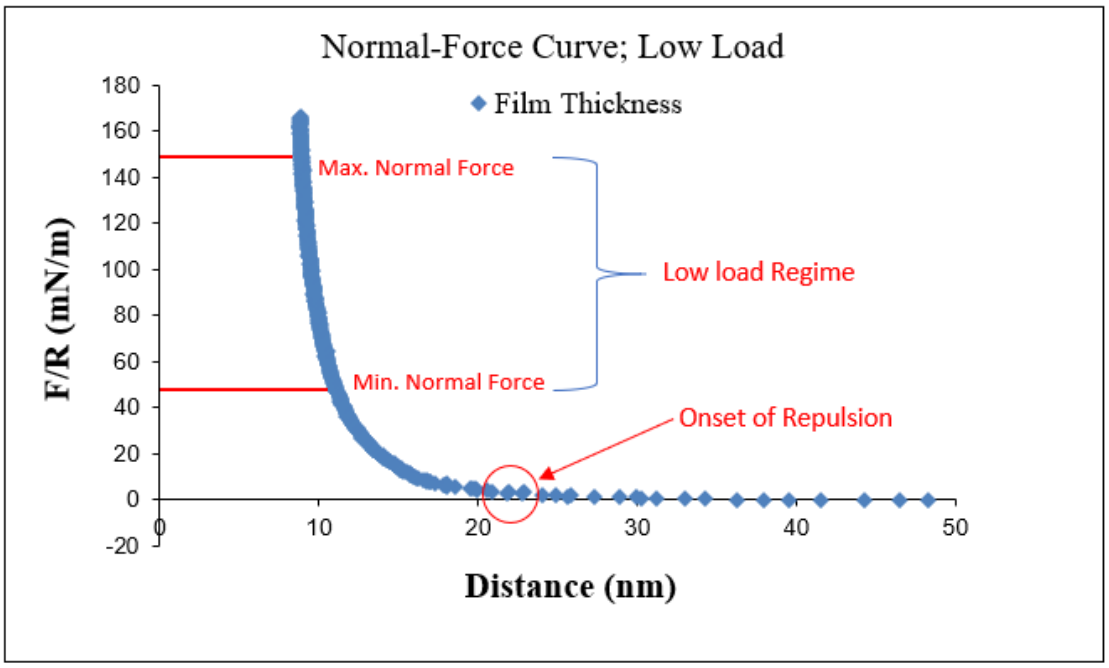

Fig. 3.1.1 Normal-Force curve for low load shearing tests showcasing the load regime for low load experiments, and the onset of repulsion

Next, we started shearing using our various protocols and monitored simultaneously the evolution of the film thickness using FECO wavelength shift (Section 3.1.2), the formation of aggregates using FECO intensity variations of fringes and newton rings (Section 3.1.3), and the resulting friction forces via our friction device (Section 3.1.4).

3.1.2 Film Thickness Evolution during Shear:

Figures 3.1.2 A→D display the evolution of the average film thickness measured during shearing experiments performed using Protocols P1, P2, P3, and P4, respectively. In all cases, the compressed film of SA showed an abrupt increase in thickness (denoted by ΔD) as soon as shear started. However, the magnitude of this increase, i.e. ΔD, varied for every protocol. As summarized in Fig. 3.1.3, ΔD was the lowest for P1 ($\Delta D \approx 18 \pm 6\, nm$) and the highest for P3 ($\Delta D \approx 85 \pm 8\ nm$), while intermediate values of $\Delta D \approx 30$, and $\Delta D \approx 37.5 \pm 3\, nm$ were measured for P2 and P4 respectively. Importantly, the large ΔD measured for P3 was in agreement with the previous SA study done in our group [1]. Following this abrupt initial increase, upon prolonged shear, the film thickness continued raising gradually in all conditions.

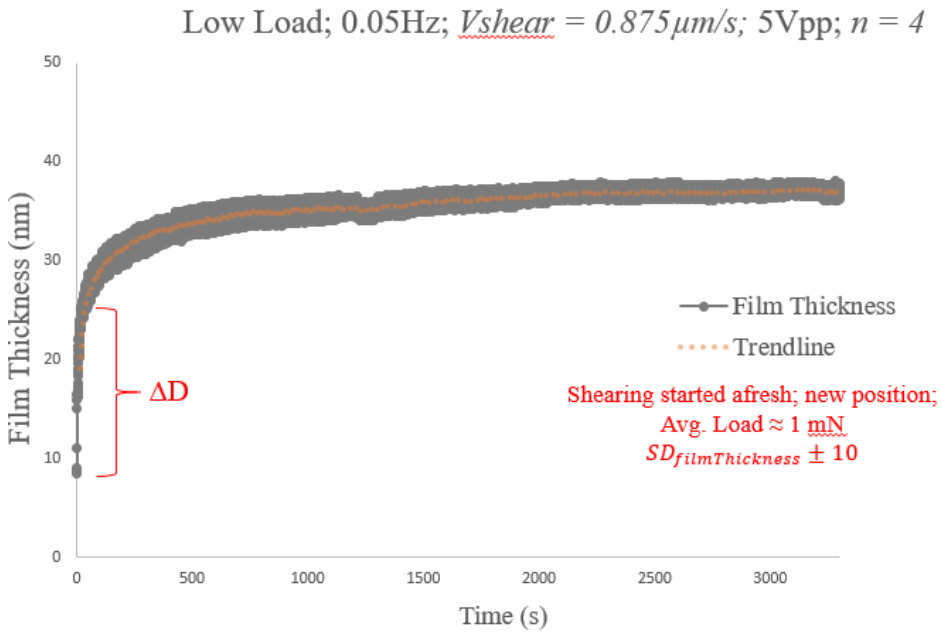
Low Load; 0.05Hz; Vshear = 0.875µm/s; 5Vpp; n = 4
Film Thickness (nm)
Time (s)
ΔD
Film Thickness
Trendline
Shearing started afresh; new position;
Avg. Load ≈ 1 mN
$SD_{filmThickness}$ ± 10

(A)

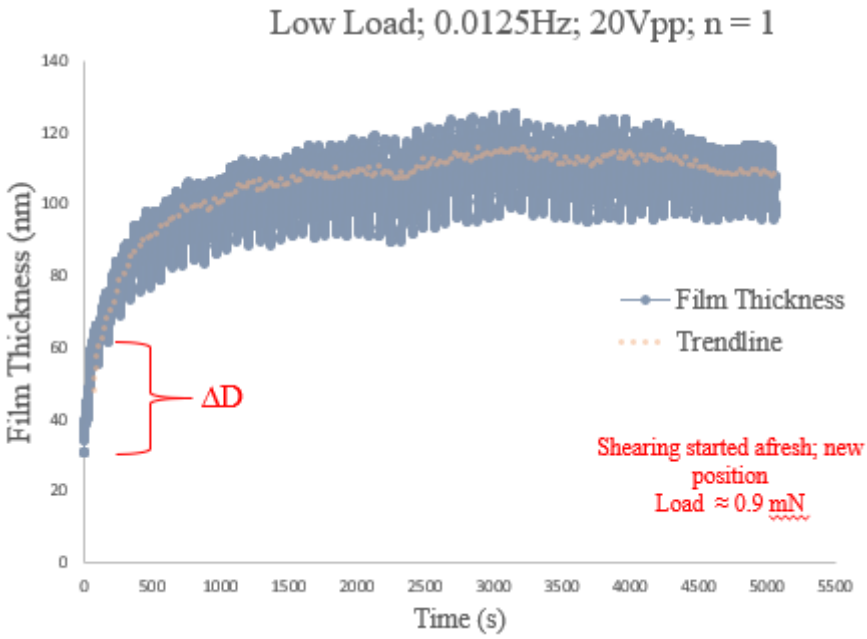
Low Load; 0.0125Hz; 20Vpp; n = 1
Film Thickness (nm)
Time (s)
ΔD
Film Thickness
Trendline
Shearing started afresh; new position
Load ≈ 0.9 mN

(B)

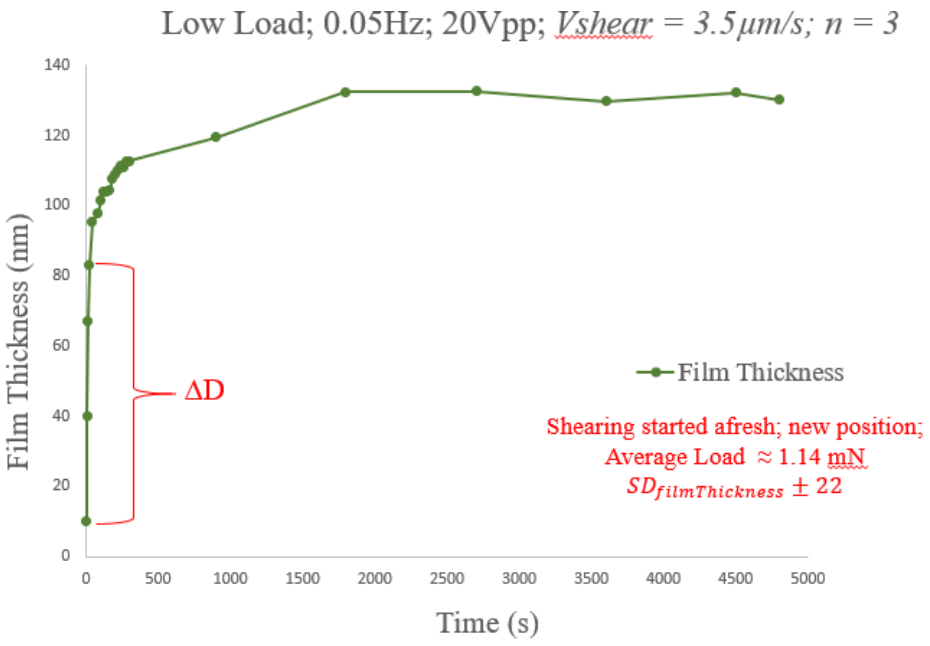

(C)

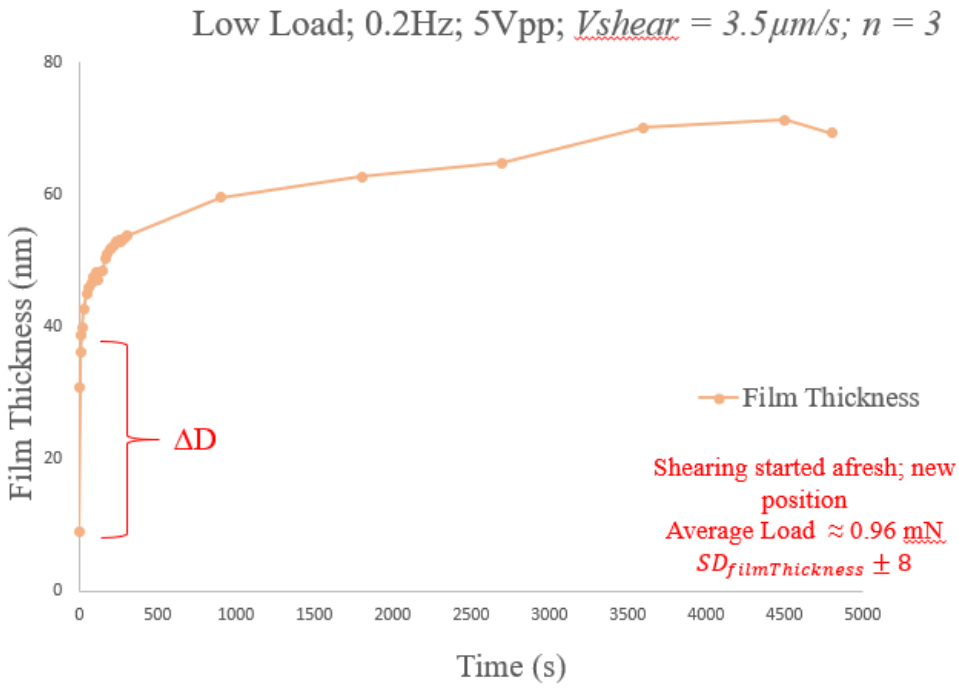

(D)

Fig. 3.1.2 Evolution of average film thickness vs. time, for shear protocol P1, n = 4 (A); for shear protocol P2, n = 1 (B); for shear protocol P3, n = 3 (C); and shear protocol P4, n = 3 (D).

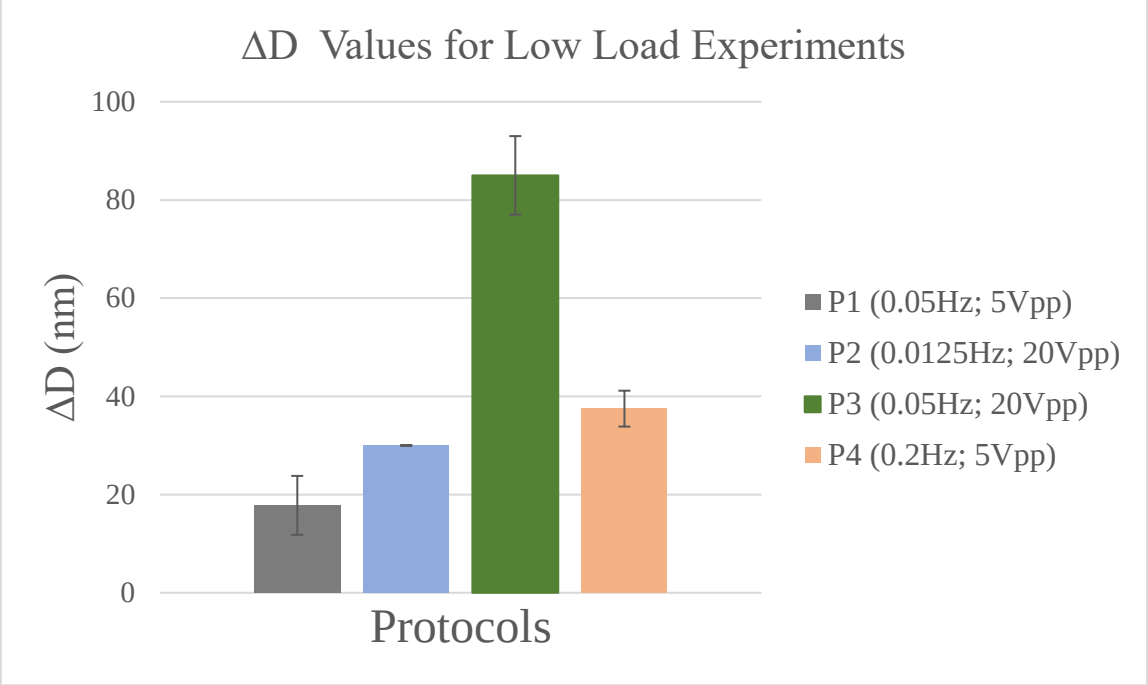

Fig. 3.1.3 Summary of abrupt film thickness increase ΔD obtained from the shearing Protocols 1, 2, 3, and 4 for low load shearing experiments

3.1.3 Dynamics of Agglomerates Formation and Surface Damage:

To test whether the above-mentioned film thickness increase was associated with the formation of aggregates, we simultaneous monitored structural changes in the sheared film by recording the variations in FECO intensity on both even and odd fringes (Fig. 3.1.4 A→D) and by capturing the Newton Rings at the end of each shearing test. Our data indicate that, except for P1 (Fig. 3.1.4 (A)), agglomerates were observed in all protocols. These agglomerates were observed as intensity alterations (ripples or discontinuities) of the even-numbered fringes, indicative of local variations in refractive index, as visible in Fig. 3.1.4 (B). When this alteration extended to the odd-numbered fringes (seen as a scratch/dark line on the FECO in Fig. 3.1.4. (C)), it was an indication either that the aggregates had grown so large that they were obstructing the light path or that the underlying mica had been damaged. The difference between mica damage and presence of very large agglomerates lies in the pattern of disturbance on the odd fringes. Over time, none of the shearing conditions we tested led to surface damage. However, among all Protocols, P3 exhibited the largest (likely rod-like) agglomerates, which were able to deform substantially the confining mica surfaces hence affecting both even and odd FECO. Such agglomerates were also observed by Banquy *et al.* in their study of shear-induced agglomeration of mammalian synovial fluid [2].

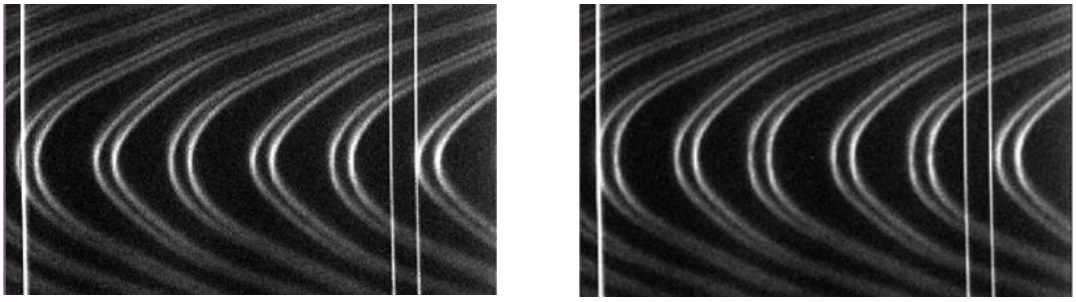

(A)

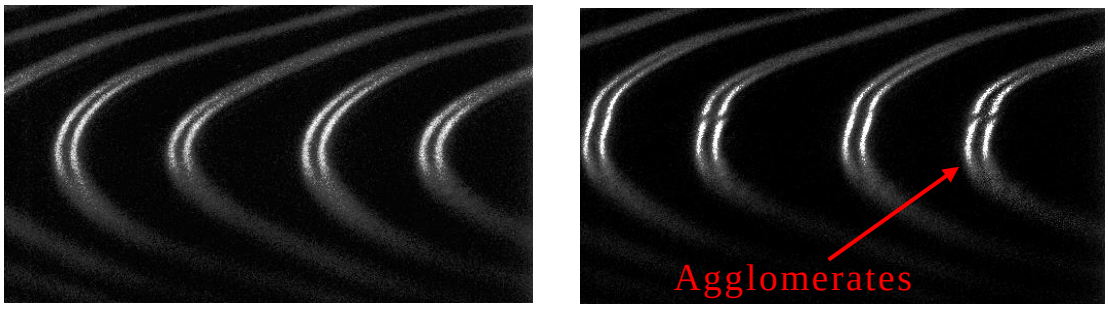

(B)

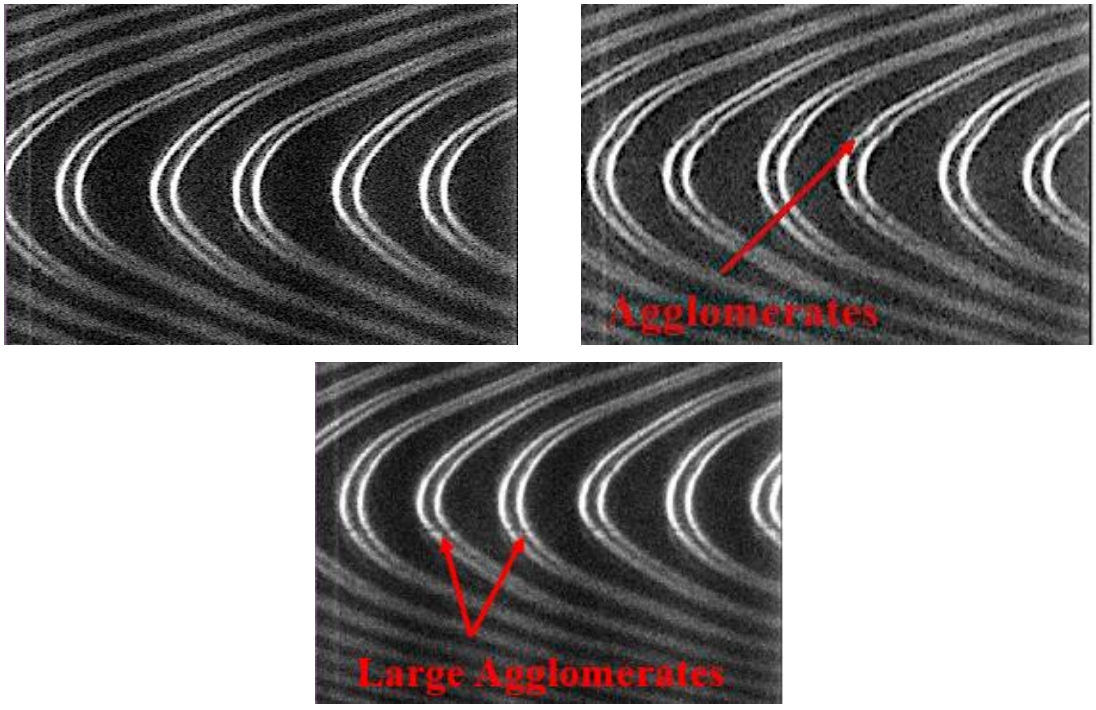

(C)

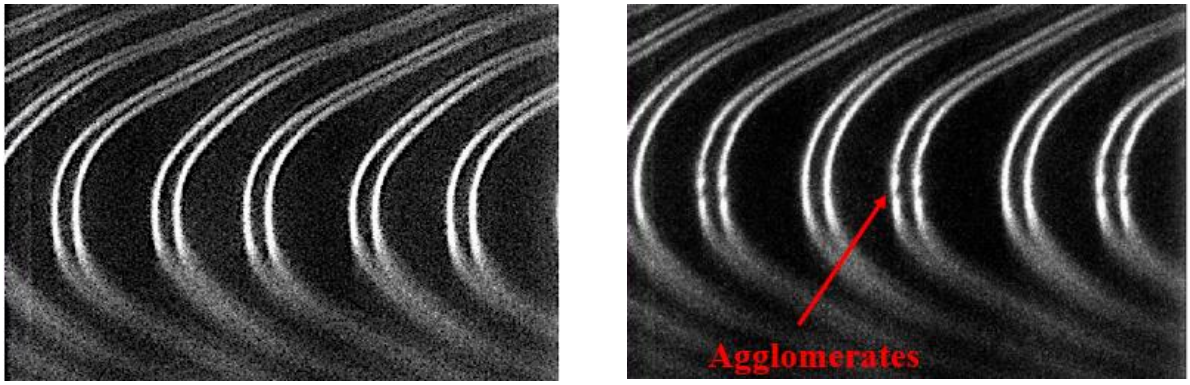

(D)

Fig. 3.1.4 (A) FECO for P1: (L – R) at the start and at the end of shearing; no aggregates observed. (B) FECO for P2: (L – R) at the start and at the end of shearing; agglomerates observed on even fringes. (C) FECO for P3: Top (L – R) at the start and at 1 hour of shearing, bottom FECO at end of shearing indicates large agglomerates, visible on both odd and even fringes. (D) FECO for P4: (L – R) at the start and at the end of shearing; agglomerates observed on even fringes.

Following shear tests, Newton rings were captured through the eyepiece to confirm the presence of agglomerates and evaluate their position and density in the sheared junction. In general, these agglomerates appear either as dark spots in the central region of the rings, or as a string of dark spots (Fig. 3.1.5). Close observation of the Newton's rings after every shearing test is necessary to avoid mistaking large 'rod-like' agglomerates (as seen in Fig 3.1.5 Left) with mica scratches (surface damage). Overall, shear-induced agglomerates were observed at the centre of the Newton's rings for all Protocols but P3.

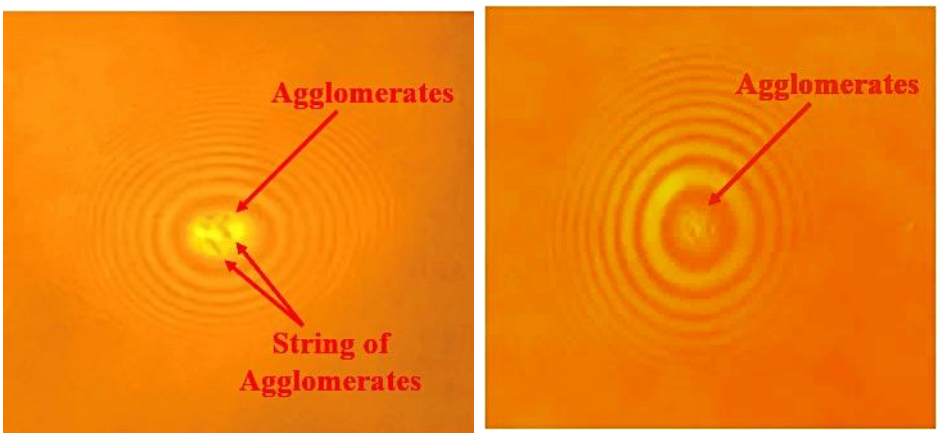

Fig. 3.1.5 (L – R) Newton's rings observed for P2 and P4 after shearing showing string of agglomerates (L) or randomly distributed agglomerates (R)

As mentioned earlier, the FECO data shown in Fig. 3.1.4 A→D indicate that, except for P1, agglomerates were observed in all protocols. However, the shearing time, number of shearing cycles, and total distance sheared before these agglomerates could form varied with Protocols. All these parameters, together with the presence/absence of damage in each Protocol have been summarized in Table 3.1.2 and will be discussed in Chapter IV.

To confirm the absence of shear-induced formation of aggregates for P1, we conducted a second normal force run on the same position after shearing was completed. The sheared surfaces were separated for an hour after one hour of shearing was concluded, and were brought back together by applying similar loads used for the shearing tests. From figures 3.1.6 and 3.1.7, we can see that the onsets of repulsion before and after the shearing test occur at similar positions. Also, the respective film thicknesses (≈ 8 nm before and ≈ 10 nm after the shearing respectively) did not show any significant difference. These similar pre and post shearing force runs strongly suggest that there were no aggregates formed in the junction. The presence of aggregates would have significantly affected both the onset of repulsion and the overall film thickness, certainly increasing the onset of repulsion distance and likely the hard wall thickness post shearing too (similar test for P3 discussed further in section 3.3).

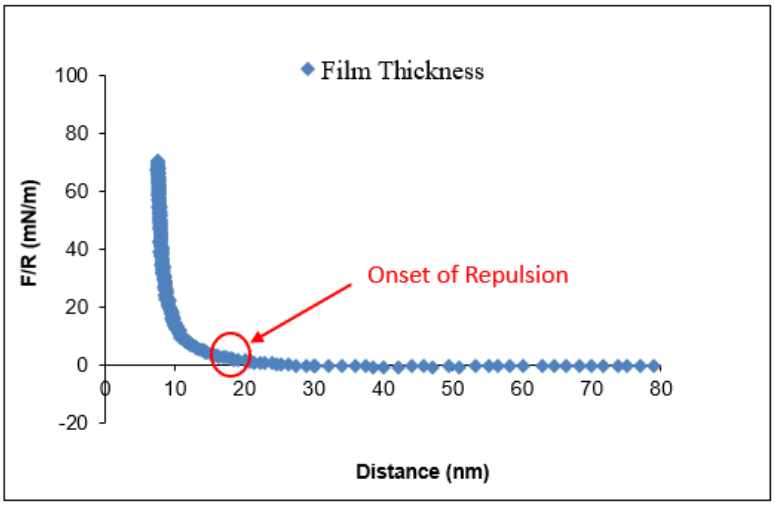

Fig. 3.1.6 Normal force – curve for P1 *before* the shearing test, indicating an onset of repulsion ≈ 19 nm.

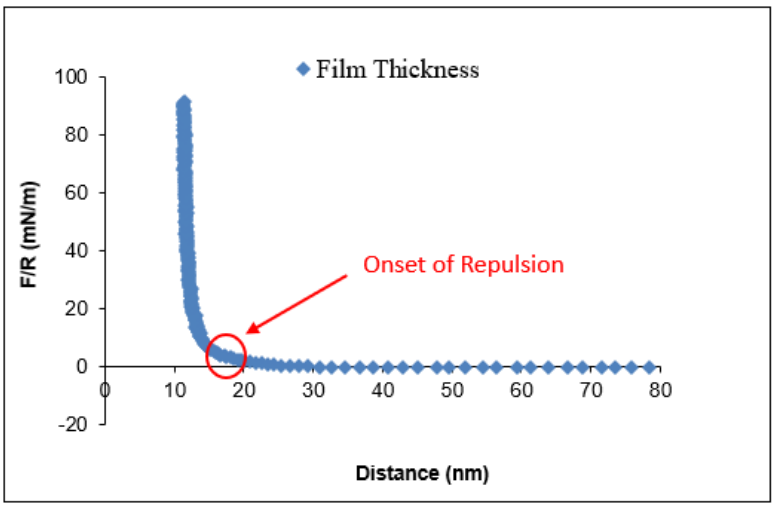

Fig. 3.1.7 Normal force – curve for P1 *after* the shearing test, with one-hour separation time between the surfaces, indicating an onset of repulsion ≈ 20 nm.

Table 3.1.2 Summary of cumulative shearing data at the onset of agglomerates formation and check for surface damage, for all protocols tested

Protocol	**Agglomerates Started to form after (Shearing Cycles)**	**Time Required for Agglomerate Formation (s)**	**Distance Covered until the Formation (m)**	**Surface Damage Observed?**
P1 (*n=4*)	No Agglomerates Observed	N/A	N/A	No
P2 (*n=1*)	≈ 5.25	≈ 420	≈ 367.5	No
P3 (*n=3*)	≈ 1.75 ± 0.1	≈ 35 ± 3	≈ 122.5 ± 13	No
P4 (*n=3*)	≈ 312 ± 13	≈ 1560 ± 68	≈ 5460 ± 238	No

3.1.4 Evolution of Friction Forces:

To test whether the presence of aggregates correlated with variations in film lubrication, we simultaneous measured the resulting friction forces (Fig. 3.1.6 A→D). While the friction force graphs for P1 and P2 displayed a steady increase with time, P3 exhibited a clear decrease and P4 a slight decrease upon time. Interestingly, our results for P1 and P2 demonstrate that, although the frictional force increased with time, no damage occurred between surfaces, indicating efficient wear-protection capability of SA. As expected, the friction force for P3 was the lowest of all Protocols, further indicating that the large 'rod-like' agglomerates formed in

the junction may act as efficient roller bearings separating the surfaces and reducing friction. Although P2 too showcased strings of aggregates (as seen in fig. 3.1.5 (L)), they were not large enough (visible on the even fringes only) to have a decreasing effect on friction.

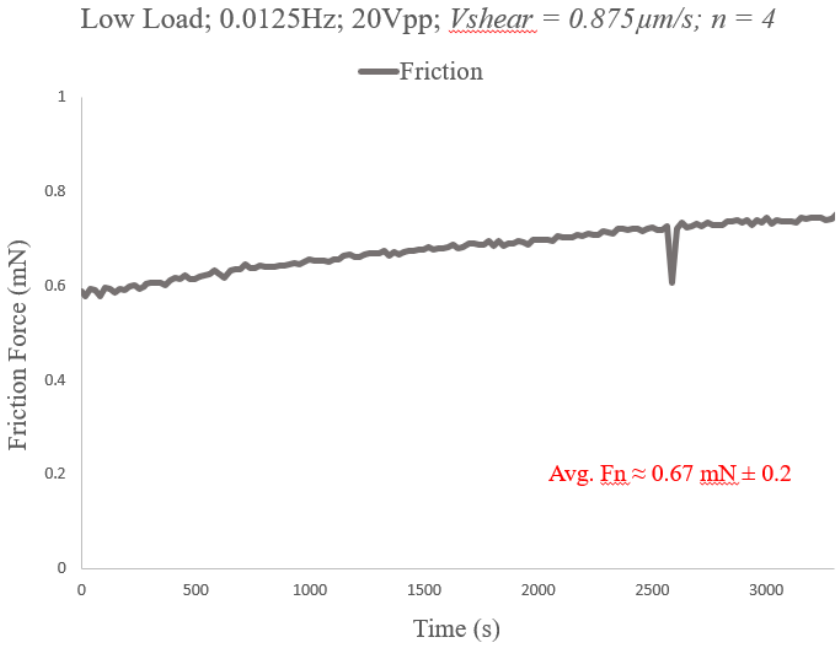

(A)

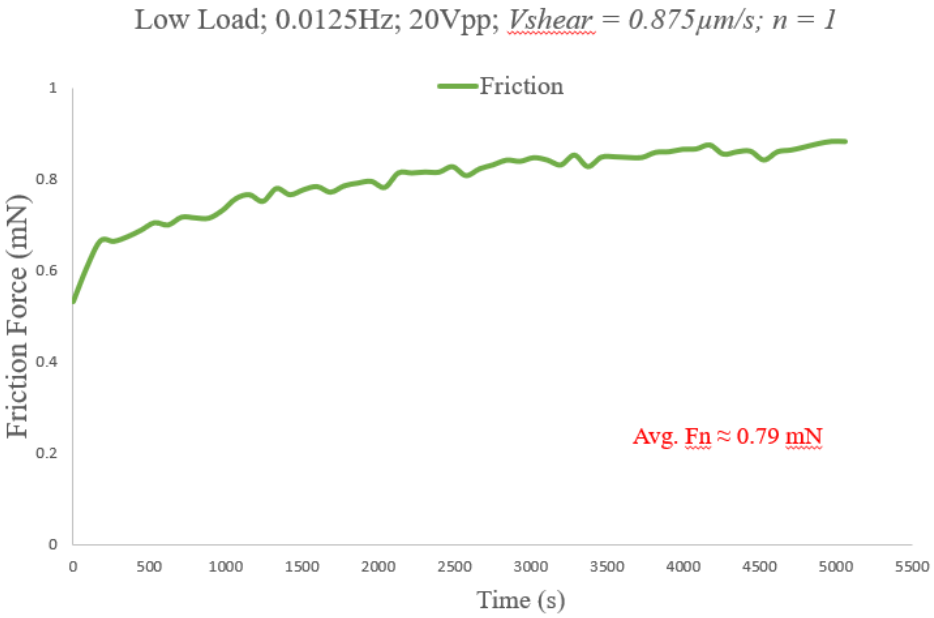

(B)

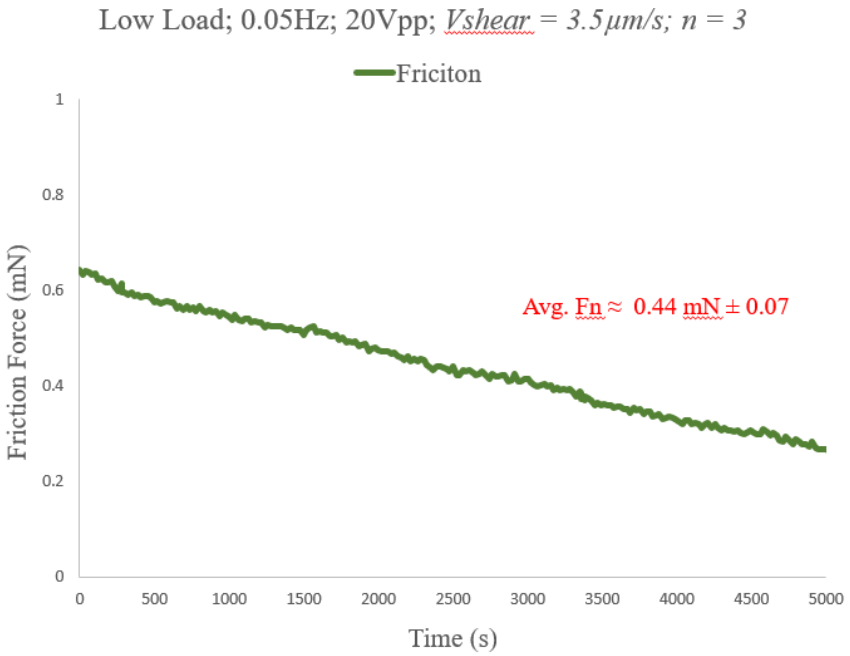

(C)

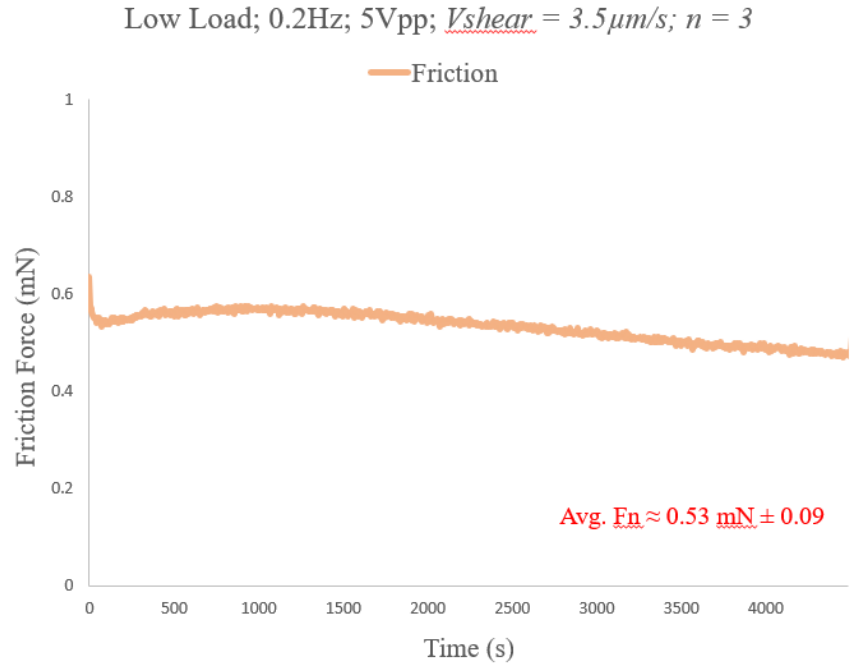

(D)

Fig. 3.1.8 (A) Average friction forces vs. time for P1,

(B) Friction force vs. time for P2, (C) Average friction forces vs. time for P3 and,

(D) Average friction forces vs. time for P4

In average, the friction forces measured were $0.6 \pm 0.2\,mN$ for P1, $0.79\,mN$ for P2, $0.4 \pm 0.1\,mN$ for P3 and $0.5 \pm 0.1\,mN$ for P4, respectively. These forces were normalized

by the corresponding normal applied loads to estimate the 'instantaneous' coefficients of friction that were found equal to $\mu_{P1} \approx 0.81 \pm 0.05$, $\mu_{P2} \approx 0.87$, $\mu_{P3} \approx 0.36 \pm 0.05$ and $\mu_{P4} \approx 0.57 \pm 0.16$.

3.2 Effect of Applied Load/Pressure:

All the experiments reported in Section 3.1 were performed under low applied loads (in the range of 0.75 to 1.25 mN. We next carried out experiments under higher load regimes to understand whether higher pressures associated with thinner sheared films would affect the formation of aggregates as well as their number. This test consisted in shearing the same position using consecutively 2 different sets of shearing parameters with the difference that only the applied load was changed while keeping *Vshear* constant. All experiments reported (n = 3) used Protocol P1 shearing parameters (5Vpp, 0.05 Hz - corresponding to a shear velocity of 0.875 $\mu m/s$). We started with shearing for one hour at low load followed by shearing for another hour at high load, with a few minutes of rest between the two sessions to (i) let the film relax and (ii) apply slowly more load using the step motor. The high loads applied were in the range of range of 4 to 7.5 mN.

3.2.1 Normal-Force Profile:

Prior to starting each high load experiment, a low load normal-force test was first conducted to measure the SA film thickness in the junction both uncompressed and in compression (data not shown here as identical to Fig. 3.1.1). Next, shear was applied for one hour under low load (reported in following Sections 3.2.2 → 3.2.4) and stopped for circa 20 minutes to let the film relax. The surfaces, however, were not separated and were still kept in contact during this relaxation period.

High load was then slowly applied on the same position using a step motor and a new normal-force test was performed, displayed in Fig. 3.2.1. The average high load applied was ≈ 4.8 mN (*n=3*). As discussed in the next sections, because the film had already been sheared at low loads, our second force run started at non-zero force and from a higher film thickness than that reported for a 'never sheared' film, due to the shear-induced thickening reported in Section 3.1. The average 'initial' thickness of the confined film after the application of high load was around 30nm.

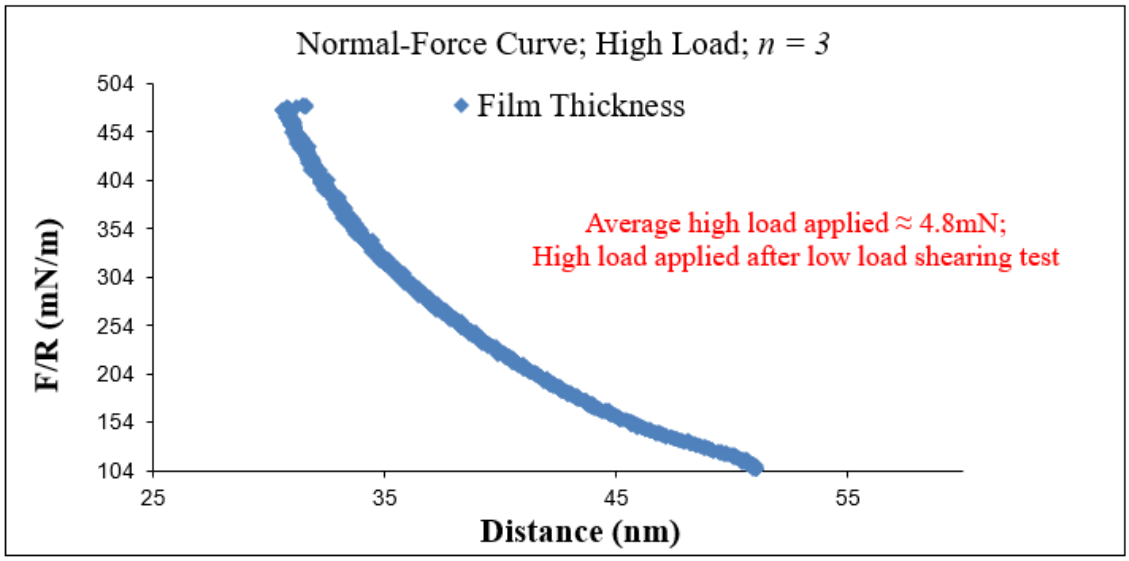

Fig. 3.2.1 High load normal-force test performed at the end of the low load shearing (first) session and prior to the high load (second) shearing session

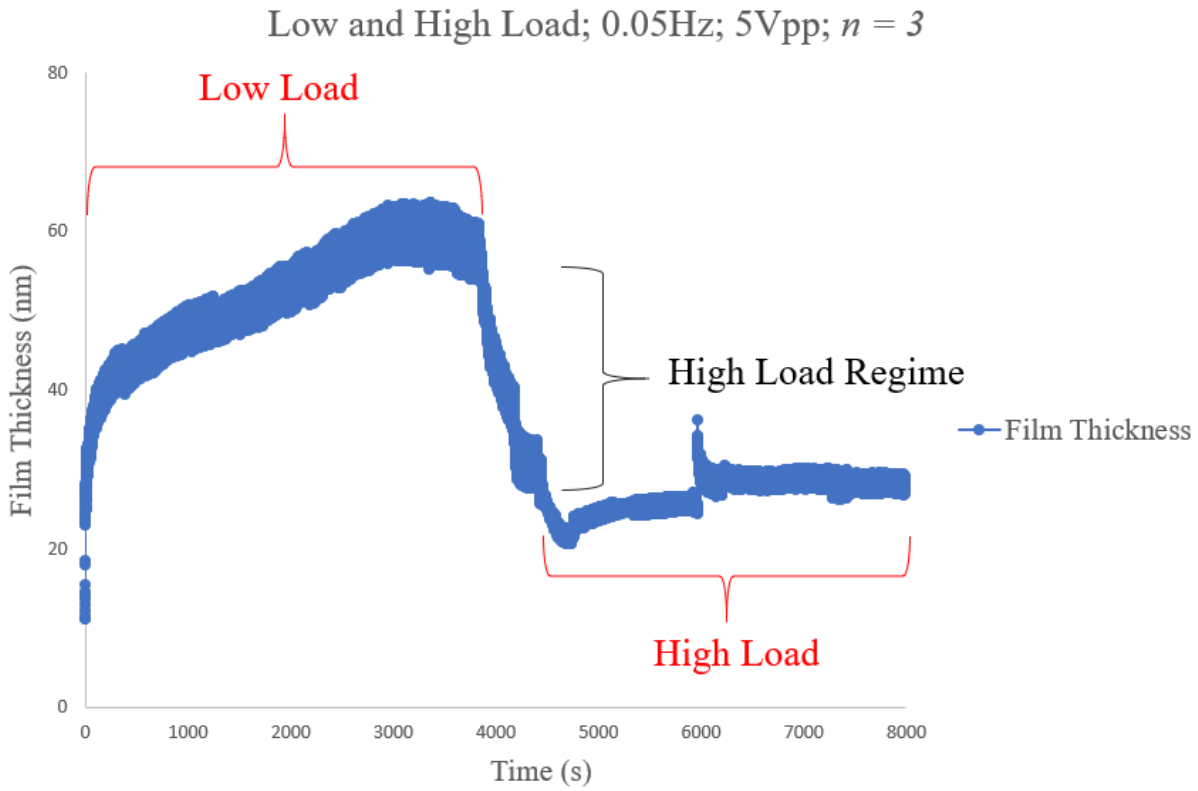

Fig. 3.2.2 Evolution of average film thickness, as measured during our low load to high load shearing regimes experiment

3.2.2 Film Thickness Evolution during Shear:

Figures 3.2.2 displays the evolution of the average film thickness measured during our low load → high load shearing regime experiment. The initial (low load) regime was similar

to the one displayed in Fig. 3.1.2, showing an abrupt thickening ΔD_{Low} of 21.5 ± 2.7 nm in average, followed by gradual thickness increase up to circa 60 nm. As shear was stopped after one hour, the film rapidly relaxed to circa 40 nm in thickness (see value at time t = 4000s).

Higher load was then applied and shear was resumed. As shear started under high load, the abrupt increase in the film thickness ΔD_{High} was much smaller than that measured at low load, and equal to circa 5 nm. The film thickness then gradually increased with time under prolonged shear and plateaued around 30 nm. Interestingly, in all high load experiments that followed low load shearing, a bulging effect was observed in the central region of the FECO, which was concomitant with the increase in load and the onset of the shearing session (Fig. 3.2.3). This bulge (Fig. 3.2.3. (B) Left) was indicative of a heterogeneously distributed film in the junction, with a thicker film portion located in the (previously sheared) central region of the junction and thinner film portion located in the (never sheared) edges of the junction. This initial bulge gradually disappeared as shear was prolonged, and FECO were completely flattened by the end of the shearing session at high load, indicative of a large contact area and a homogeneously distributed confined film in the whole sheared junction (Fig. 3.2.3. (B) Right).

3.2.3 Monitoring Agglomerates Formation and Surface Damage:

Similar to low load shearing experiment reported for P1 in Section 3.1.3., even when subjected to high loads, the film did not show any signs of agglomeration nor damage, as indicated by unaltered FECO during both low and high load regimes prior and after shear (Figs. 3.2.3 A→B). The only difference being the bulge discussed above in Section 3.2.2.

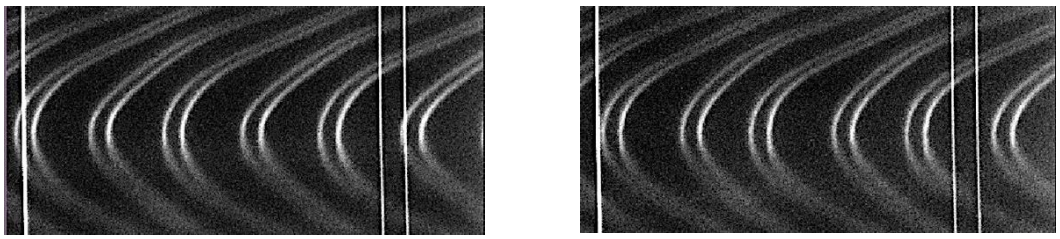

(A)

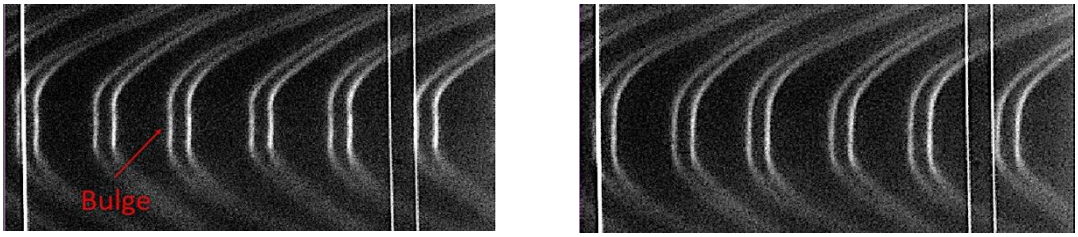

(B)

Fig. 3.2.3 (A) FECO for Low-load part of the experiment; (L – R) at the start and at the end of shearing test. No signs of agglomerates seen on the fringes, and (B) FECO for High-load part of the experiment; (L – R) at the start and at the end of shearing test. No signs of agglomerates seen on the fringes. Bulging effect observed at the onset of shearing.

3.2.4 Evolution of Friction Forces:

As expected, the average friction force increased from circa 0.35 mN at low load to 1.6 mN at high load (Fig. 3.2.4), corresponding to coefficients of friction from $\mu_{low} = 0.45$ to $\mu_{High} = 0.3$. Interestingly, even under high loads, SA still produced remarkably low values of coefficient of friction without any surface damage, confirming its ability to protect efficiently surfaces from wear when sheared past each other.

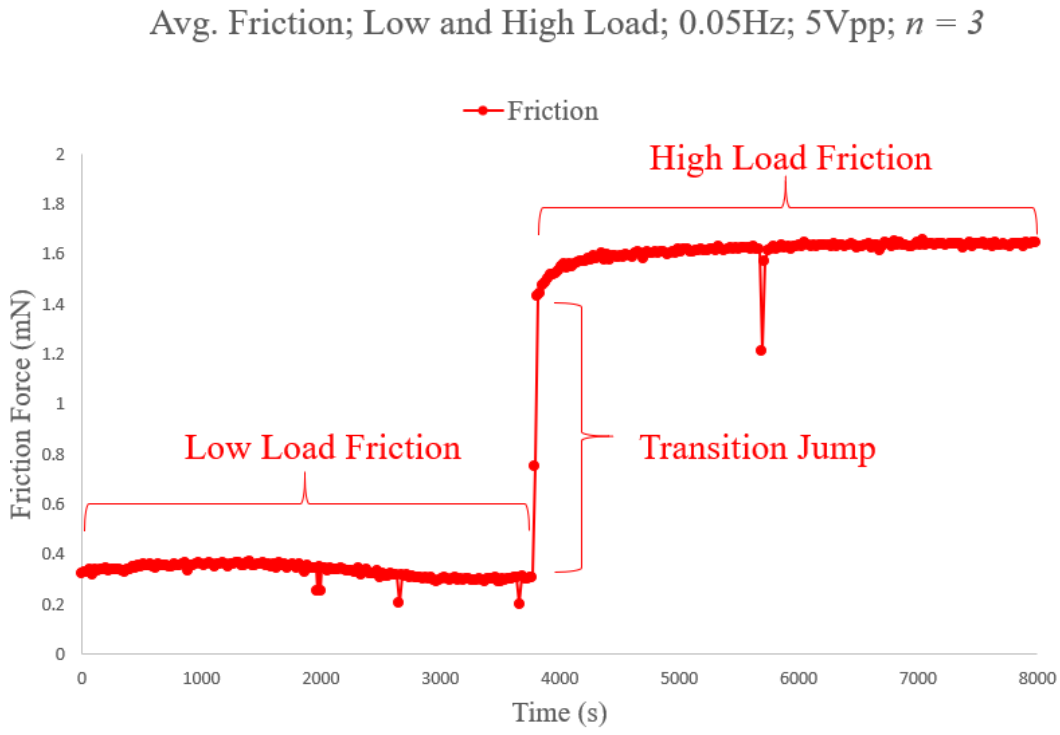

Fig. 3.2.4 Average friction forces, as measured during our low load to high load shearing regimes experiment

Here, we would like to mention that although protocol P1 was used for the low load part of the experiments, the average friction force measured was lower than that observed for P1 experiments discussed in section 3.1.4. This was likely caused by one of the experiments we performed (from section 3.1) that yielded unexpected high friction due to longer exposure of the film to white light in the SFA setup, which accelerated film dehydration and made it more viscous prior to measurements. This in-turn increased the average friction value for P1 (discussed in section 3.1.4).

3.3 Effect of Strength of Attachment of SA to Surfaces:

In all the experiments reported so far in Chapter III, fibronectin (FN) was systematically deposited onto mica prior to incubation of the surfaces in SA solutions. This is because FN, a glycoprotein present in the superficial zone of the cartilage, was found capable of anchoring various SF constituents (among which SA) to mica, hence maintaining them within the contact junction during shear, even under high loads and high speeds [3]. To test whether strength of attachment affects aggregate formation and overall lubrication by SA, we next performed SA experiments without pre-coating our mica with FN. We focused on P3 shearing conditions at low loads (in the range of $1 - 1.5$ mN) and monitored FECO (aggregates formation), film thickness and friction of both FN+SA and 'SA only' films, with the aim of identifying differences in aggregates structure, density, stiffness, longevity, and over all pattern of formation.

We first noticed that aggregates appeared earlier (at lower shearing times) in FN+SA films than in SA films. Additionally, as seen in Figs. 3.3.1 (A) and 3.3.1 (B), agglomerates observed in FN+SA films seemed to appeared more numerous, and denser than those in SA 'only' films, as indicated by larger and more frequent FECO dark bands visible in both even and odd ordered fringes. These data show that FN strongly affects the shear-transformation of SA within the surfaces, in particular onset of aggregate formation as well as size and density of aggregates.

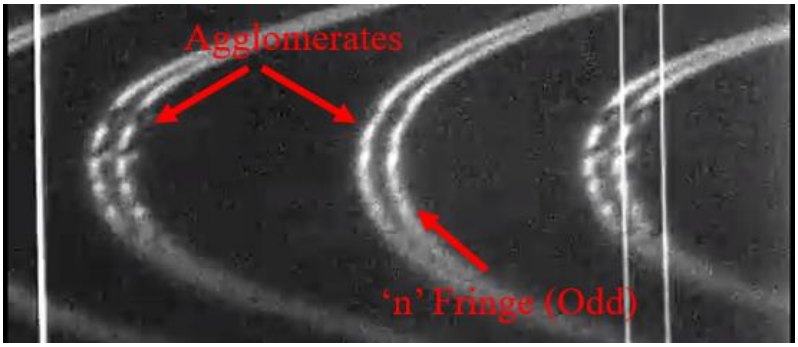

(A)

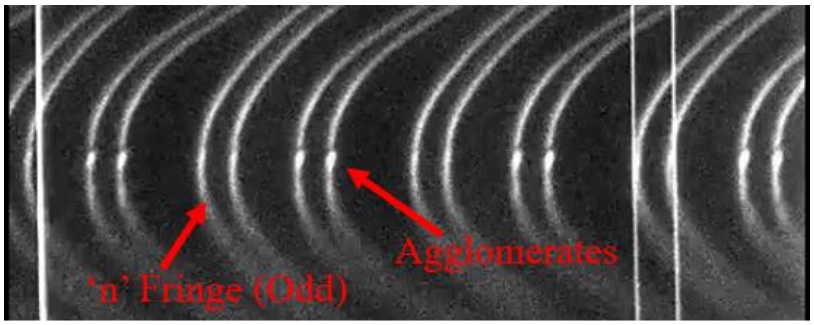

(B)

Fig. 3.3.1 (A) Agglomerates seen on both the even and the odd fringes for FN+SA films, after one hour of shear (P3 conditions), and (B) Agglomerates seen mainly on the even fringes for 'SA only' films, after one hour of shear (P3 conditions).

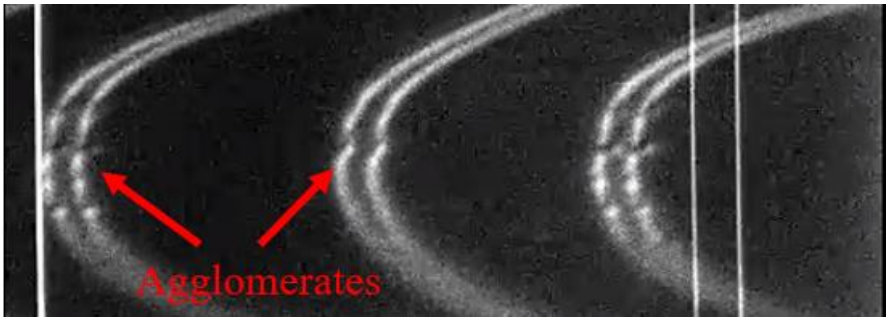

(A)

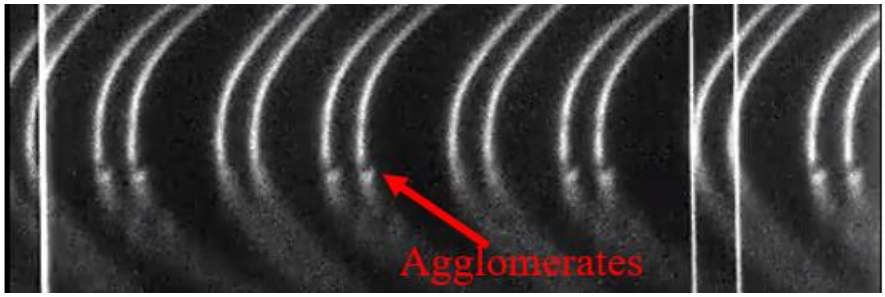

(B)

Fig. 3.3.2 (A) Agglomerates can still be seen on both even and odd fringes for FN+SA experiment after a separation time of 1 hour, indicating long-lived structures (B) Agglomerates can still be seen on the even fringes for 'SA only' experiment after a separation time of 1 hour; additionally they seem to be displaced towards the lower half of the fringes compared to their position at the end of the shearing test (Fig. 3.3.1)

We next estimated the longevity of the aggregates formed in FN+SA and SA films. To do so, we stopped shearing, separated the surfaces by circa 1 mm, kept them apart for one hour, then brought them back in contact at the exact same position and under same applied load than during the previous shearing session. Our FECO data (Figs. 3.3.2 (A) and 3.3.2 (B)) indicate that, in both FN+SA and 'SA only' cases, agglomerates do not dissolve when the films are immersed back in a SA solution reservoir, instead, they subsist and stay anchored to the previously sheared surfaces, at least under low applied load. Since no clear difference was observed between FN+SA and 'SA only' aggregates at this point, we next increased the load up to circa 2 mN and could observe a displacement of some aggregates from the center to the edge of the junction in the case of 'SA only' films, as observed by monitoring the dark band on even fringe from Fig. 3.3.1 (B) (central position of FECO) to Fig. 3.3.2 (B) (lower side of FECO). These results indicate that SA films, and associated aggregates formed, tend to be more loosely bound to the confining mica surfaces, which affect their tribological behaviour. Next, we attempted to compare the size of FN+SA and 'SA only' aggregates by plotting the force curves obtained after shearing and 1h separation (Fig. 3.3.3). The onset of repulsion occurred at a larger distance (≈ 210nm) for 'SA only' films compared to that of FN+SA (≈ 130nm), suggesting that SA aggregates might be larger than their FN+SA counterpart; however, only one experiment was performed and more data are definitely needed to validate our findings.

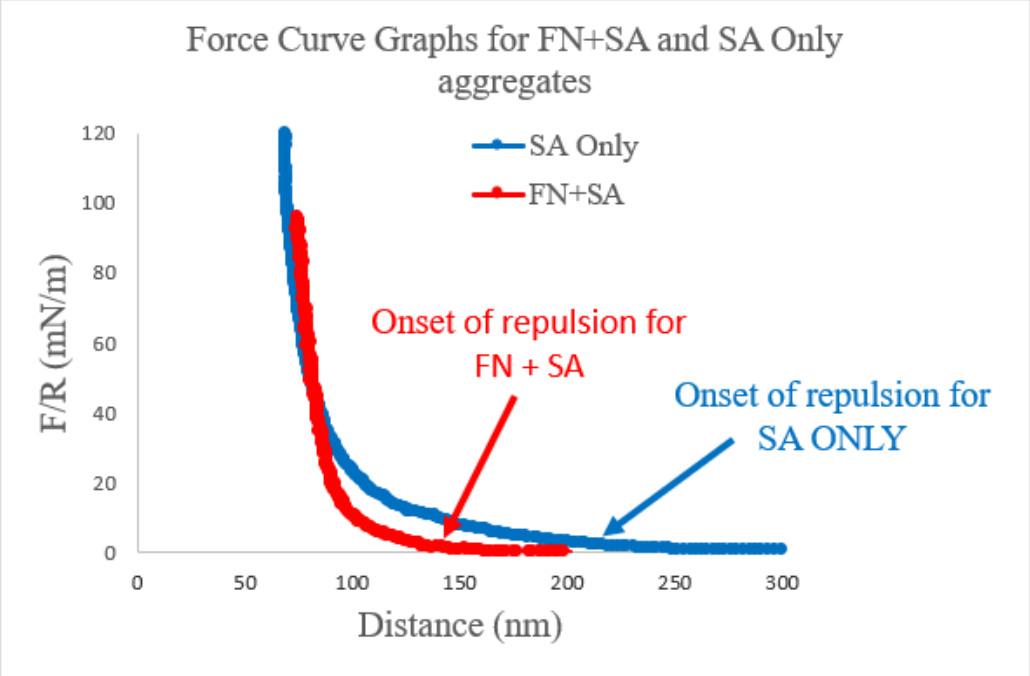

Fig. 3.3.3 Normal force – curves for SA only and FN + SA films after the shearing test.

3.4 Effect of Previous Shearing History:

To study the effect of previous shearing history on the shear-transformation of SA films, we extended the FN+SA and 'SA only' experiments reported in Section 3.3. and focused specifically on the effect of previous shear on the evolution of both the number and the structural properties of aggregates formed, when a new shearing session of circa 15 minutes was performed at the same position, after 1 hour of surface separation at rest. We noticed that, as shear was resumed, FN+SA agglomerates tended to grow larger in the junction, as indicated by the larger alterations (compared to those observed during the first part of shearing) of FECO intensity visible in both even and odd fringes, suggesting either growth of aggregates and/or coalescence of existing aggregates into larger agglomerates able to obstruct light path (Fig. 3.4.2 (A)). In contrast, 'SA only' aggregates did not appear to get significantly larger in comparison to their size observed in the first part of shearing, however, resuming shear enhanced the effect previously mentioned in Section 3.3 when high load was applied, namely it led to the further displacement of some aggregates from the center to the edge of the junction (Fig. 3.4.2 (B)). This loose attachment of aggregates in 'SA only' was also evident in the normal force – curves carried out after the first part of shearing (Fig. 3.3.3).

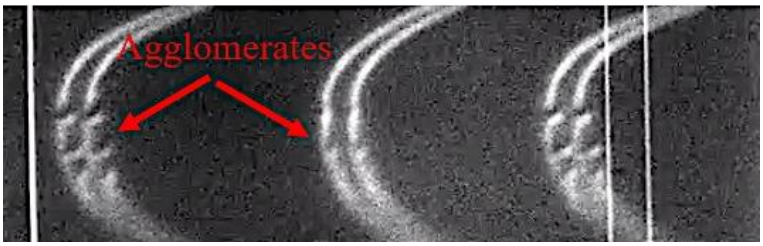

(A)

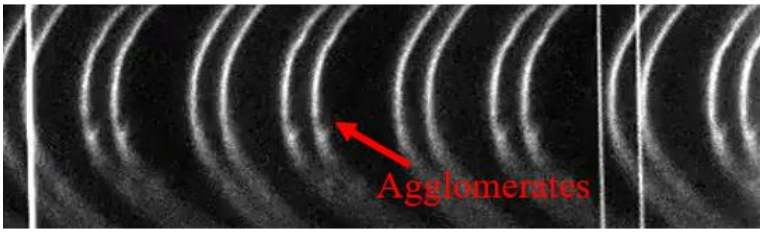

(B)

Fig. 3.4.1 (A) Agglomerates seen on both even and odd fringes in FN+SA films, when shear was resumed for 15 minutes after a separation time of 1 hour, and (B) Agglomerates seen exclusively on even fringes in 'SA only' films, when shear was resumed for 15 minutes after a separation time of 1 hour

3.5 Statistical Analysis:

Statistical analysis was performed on the gathered data of the shearing tests performed on normal loads between 0.75 to 1.25 mN (discussed in section 3.1) using Minitab.

3.5.1 Statistical Analysis for ΔD Phase:

Multiple regression analysis was carried out on all the ΔD values (ref. table 3.5.1) measured for P1 (n = 4), P2 (n = 1), P3 (n = 3), and P4 (n = 3) protocols, with shearing cycles and shearing amplitude as controlled variables. The P – value achieved for both shearing cycles and shearing amplitude was < 0.001. While those for R – squared (R – sq), R – squared (adjusted), and R – squared (predicted) were measured at 93.89%, 92.36%, and 81.82% respectively. Based on the analysis, the regression equation was given as follows:

$$\Delta D = 17.61 - 0.952\ Shearing\ Cycles\ seconds + 1.233\ Shearing\ Amplitude\ um$$

From the analysis results, it can be seen that both, shearing cycles and shearing amplitude, were statistically significant as the P values were < 0.001 at 99.9% i.e. ΔD did significantly depend on both shearing cycles and amplitude. R – sq value of 93.89% shows that

93.89% of variation in ΔD can be explained by the two experimental factors shearing cycles and shearing amplitude. The remaining of variation i.e. 6.11% is random. Also, R-sq (predicted) value of 81.82% suggests that the model has predictability of 81.82% for new values of the two variables. As R-sq (adjusted) value of 92.36% is close to R-sq value, we can confidently say that the model does not show any concern. Main effects plot (Fig. 3.5.1) and contour plot (Fig. 3.5.2) from the analysis explain the effects of the two variables (shearing cycles and shearing amplitude) on mean predicted ΔD, and the predicted values of ΔD with the regression model respectively. From the contour plot it can be seen that predicted ΔD is the lowest when sharing cycles is the highest and shearing amplitude is the lowest, while it is the highest when shearing cycles is the lowest and shearing amplitude is the highest.

Table 3.5.1 Data table for regression analysis with respective ΔD values for each experiment

Protocols	**Shearing cycles (s)**	**Shearing Amplitude (µm)**	**Delta D (nm)**
P1	20	17.5	8
P2	80	70	30
P3	20	70	70.88
P4	5	17.5	38.7
P1	20	17.5	18
P3	20	70	91.85
P4	5	17.5	32.5
P1	20	17.5	21.4
P3	20	70	89.52
P4	5	17.5	41.2
P1	20	17.5	24

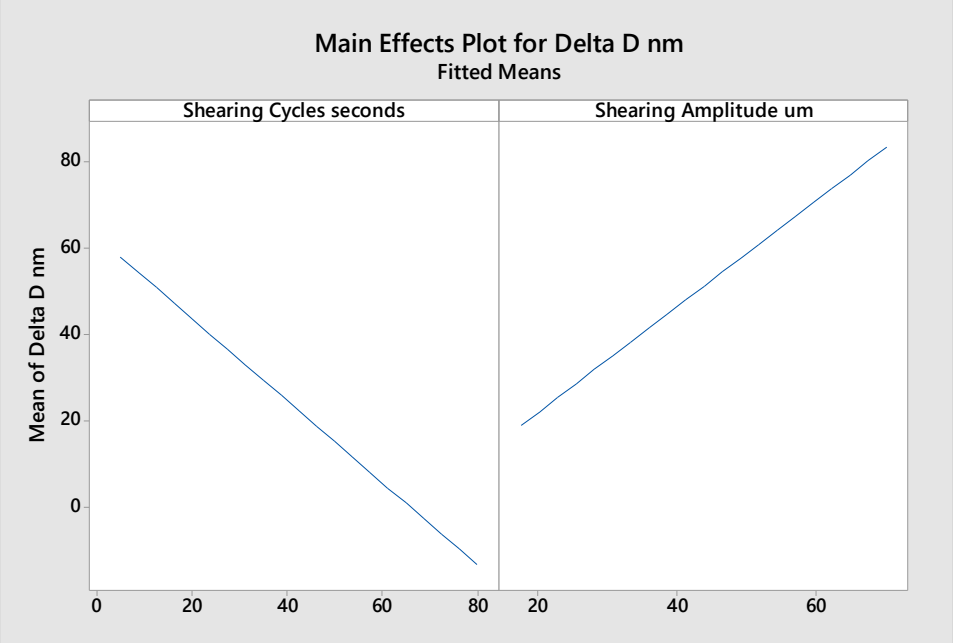

Fig. 3.5.1 Main effects plot showing the effect of shearing cycles and shearing amplitude on mean predicted ΔD

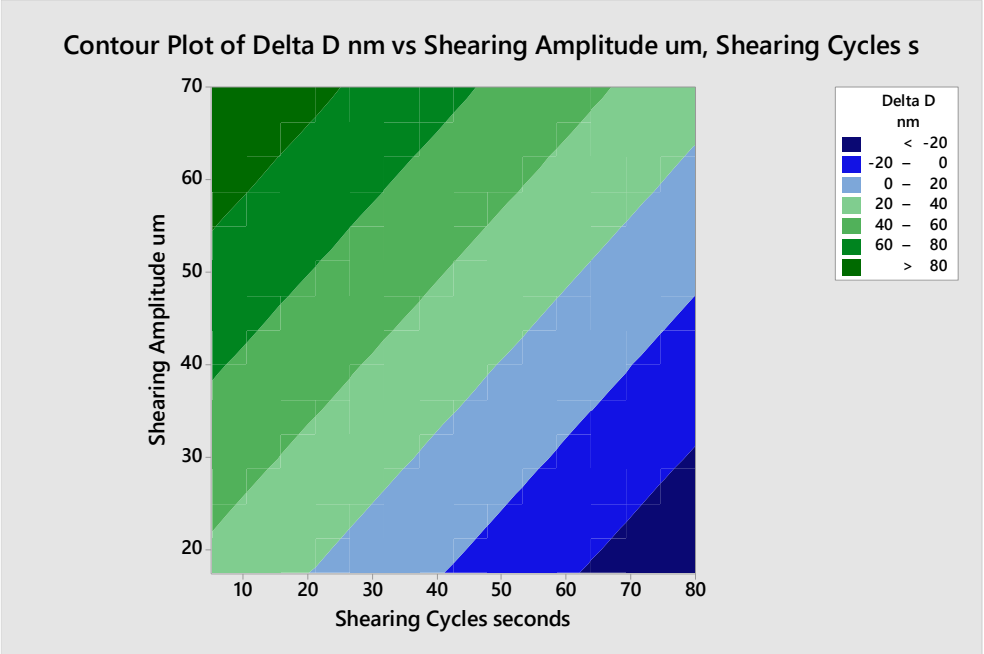

Fig. 3.5.2 Contour plot showing the predicted ΔD values using the regression model

The regression model signifies that ΔD is influenced by both shearing cycles and shearing amplitude, and that its predicted value increases upon decrease in shearing cycles and increase in shearing amplitude and vice versa.

3.5.2 Statistical Analysis for Protocols (Low Load Tests):

As the data was not normally distributed, Mann – Whitney nonparametric test was carried out, instead of a t-test, for P1 and P2, and P3 and P4 to see if they were different (observations in one sample larger than those from the other) or are similar (both samples come from the same population), and Kruskal – Wallis nonparametric test was carried out, instead of an ANOVA test, on P1, P2, P3, and P4.

For both Mann – Whitney tests i.e. for P1 and P2, and P3 and P4, the P values achieved were < 0.001 at 95% confidence, there by indicating that P1 was significantly different from P2, and P3 that from P4. The Kruskal – Wallis test also yielded a P value that was < 0.001 for both adjusted and non – adjusted ties, indicating that P1, P2, P3, and P4 were significantly different from one another.

3.5.3 Statistical Analysis for Aggregate Formation:

Multiple regression analysis was carried out on the values measured for the shearing cycles when the aggregates started to be visible on the FECO in P2 (n = 1), P3 (n = 3), and P4 (n = 3) protocols, with shearing cycles and shearing amplitude as controlled variables. Following is the experimental data summary table. As P1 did not show any signs of aggregates, its 'Y' value i.e. Aggregates shearing cycles (number of cycles measured when the aggregates started to show on the FECO) was not included in the data. The P value achieved for shearing cycles was > 0.001 while it was < 0.001 for shearing amplitude. This result signifies that, from the experimental data provided for the analysis, aggregates shearing cycles significantly depend on shearing amplitude and not shearing cycles. As a result, another multiple regression test with $\lambda = 1$ was carried out with only shearing amplitude as the controlled variable. Since the residual variance was increasing significantly in the regression test with $\lambda = 1$, we did a box-cox optimal lambda transformation, where the λ value chosen was 0.5. The regression equation based on the analysis is as follows:

Aggregate Shearing Cycles^0.5 = 23.024 - 0.30658 Shearing Amplitude

The residual plots (Fig. 3.5.3) after the box-cox transformation improved and showed reasonably normal distribution implying no concern on the validity of the regression model. The R – sq value achieved was 99.74%, meaning that 99.74% of variation in Aggregate shearing cycles can be explained by the one experimental factor which is shearing amplitude. The remaining of variation i.e. 0.26% is random. The values for R – sq (predicted) and R – sq

(adjusted) values achieved were 99.48% and 99.68% respectively. R – sq (predicted) suggests that the model has predictability of 99.48% for new values of the two variables, while as R – sq (adjusted) value is close to that of R – sq, thus the model does not show any concern. The Main Effects plot (Fig. 3.5.4), which shows the effects of shearing amplitude on the mean predicted aggregates shearing cycles, indicates that as shearing amplitude is increased, the mean of predicted aggregate shearing cycles decreases i.e. with increase in shearing amplitude, the aggregates presence/formation time (as seen on the FECO) decreases.

Table 3.5.2 Data table for regression analysis with respective aggregates shearing cycle values for each experiment

Protocols	**Shearing cycles (s)**	**Shearing Amplitude (µm)**	**Aggregates shearing cycles**
P1	20	17.5	*
P2	80	70	5.25
P3	20	70	2
P4	5	17.5	315
P1	20	17.5	*
P3	20	70	1.7
P4	5	17.5	327
P1	20	17.5	*
P3	20	70	1.55
P4	5	17.5	294
P1	20	17.5	*

The regression model signifies that aggregates shearing cycle statistically depend on shearing amplitude alone, and that its value is inversely proportional to shearing amplitude, i.e. upon increase in shearing amplitude reduces the value of aggregate shearing cycles and vice versa. Here, we would like to mention that although the regression model shows the relationship between the shearing amplitude and aggregates shearing cycles, it does not take into account the shearing velocity (*Vshear*) i.e. time. This was because P2 experiment was carried out only once, and that P1 showcased no aggregates.

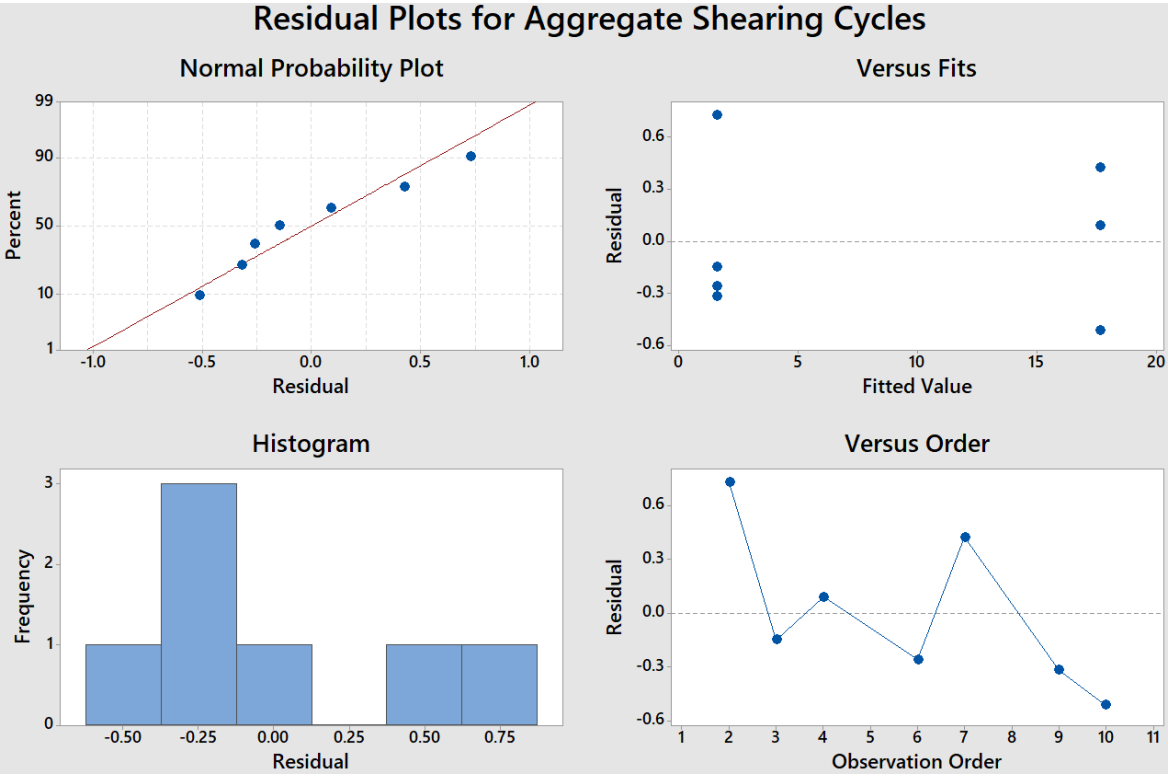

Fig. 3.5.3 Residual plots for aggregate shearing cycles after the box – cox transformation; shows reasonably normal distribution

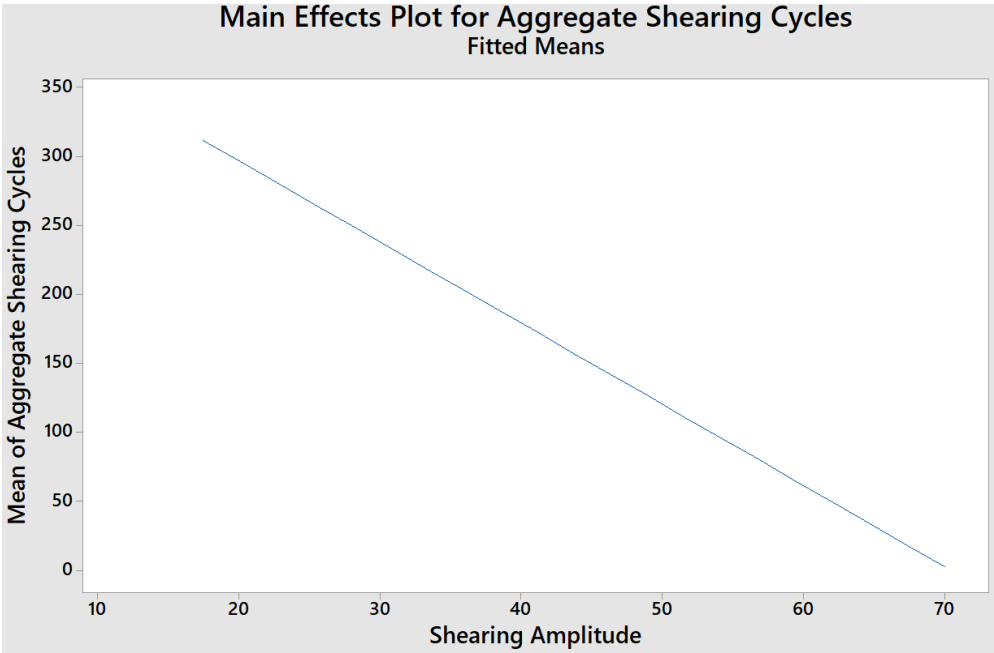

Fig. 3.5.4 Main effects plot for aggregate shearing cycles; showcases its effect on mean of predicted aggregate shearing cycles

3.6 References

[1] S. G. Cook, Y. Guan, N. J. Pacifici, C. N. Brown, E. Czacko, M. S. Samak, L. J. Bonassar, and D. Gourdon "Dynamics of Synovial Fluid Aggregation under Shear," in revision at *Langmuir* (Special issue Intermolecular Forces and Interfacial Science), 2019.

[2] X. Banquy, D. W. Lee, S. Das, J. Hogan, and J. N. Israelachvili, "Shear-induced aggregation of mammalian synovial fluid components under boundary lubrication conditions" *Adv. Funct. Mater.*, vol. 24, no. 21, pp. 3152–3161, 2014.

[3] R. C. Andresen Eguiluz, S. G. Cook, C. N. Brown, F. Wu, N. J. Pacifici, L. J. Bonassar, and D. Gourdon, "Fibronectin mediates enhanced wear protection of lubricin during shear" *Biomacromolecules*, vol. 16, no. 9, pp. 2884–2894, 2015.

Chapter - IV : Discussion

In this thesis, we used the SFA to elucidate the evolution of albumin films under shear. We monitored film thickness and film structural changes while simultaneously measuring friction forces when the films were subjected to a large range of shearing conditions (varied shearing parameters, varied loads, varied adhesion strength to surfaces with history of shearing). Overall, we found that, in most of the shearing conditions tested, SA films would (i) abruptly thicken, (ii) form long-lived aggregates that would grow bigger and/or coalesce with time, (iii) exhibit low friction and (iv) ensure absence of damage of the sheared surfaces. However, different shearing conditions led to differences in the dynamics of formation of aggregates as well as in their density and mobility at surfaces. The effect of the various shearing parameters we have tested and the implications of our results in both implant and joint lubrication are discussed in the following sections.

4.1 Effect of Attachment Strength of SA to Mica – Role of Fibronectin:

To study the effect of the strength of SA attachment to mica on agglomerates formation, we used two types of systems: first, SA was attached to mica via an intermediate layer of fibronectin (FN); second, SA was directly physisorbed to mica. As mentioned in chapter III (section 3.3), FN was used in previous SFA studies to efficiently anchor various synovial fluid components (e.g., albumin, hyaluronan, lubricin) to mica surfaces, which would prevent them from being expelled from the sheared junction, even when high loads were applied [1]. Our FECO imaging and normal force measurements (Figs. 3.3.1 (A) and (B)) indicate that SA molecules formed denser and larger number of agglomerates in the shearing junction when they were strongly anchored to mica (in presence of FN, i.e., in so called FN+SA films) than when they were loosely attached (no FN, i.e., in so called ‘SA only’ films). While, upon shearing the same position again (i.e. having a shearing history) the agglomerates seemed to grow in size for FN+SA films compared to ‘SA only’ films (Fig. 3.4.1 (A) and (B)). Another difference we observed was in the dynamics of formation of aggregates, with FN+SA films showing faster aggregation (occurring after shorter shearing times) than ‘SA only’ films. Additionally, our FECO data prior and after rest (post shear) show that, once they were formed, the lifespan of the agglomerates did not seem to depend on initial strength of attachment of SA to mica, indicating strong and irreversible interactions between SA molecules within aggregates, independently of the presence of FN. However, we noticed that the mobility of the

aggregates formed differed between systems, with ‘SA only’ aggregates able to be displaced and roll out of the junction (Fig. 3.3.1 (B) and 3.3.2 (B)).

Although multiple mechanisms might be simultaneously responsible for SA aggregation, pressure and/or shear stress-mediated protein denaturation seems consistent with the abrupt formation of aggregates observed in our study [1]. Additionally, the differences in structural (number, size, density) and mechanical (stiffness) properties of aggregates formed, as measured in both our SA and FN+SA films reinforce the idea of irreversibly entangled structures composed either of denatured SA or denatured SA entangled with FN, respectively, and stabilized by strong hydrophobic interactions consequent to the exposure of the proteins’ cores. In fact, previous studies in our group reported that the conformation of most FN molecules upon their adsorption on SFA curved mica surfaces is partially unfolded [2]. This partially unfolded conformation promotes the exposure of its cryptic binding sites. Furthermore, the presence of SA was shown to instigate the exposure of other hydrophobic sites on FN [3], leading to further unfolding of FN, which could explain why FN+SA films form more instantaneous aggregates. Finally, both the shorter times needed to form aggregates in FN+SA films compared to ‘SA only’ films and the higher mobility of ‘SA only’ aggregates are consistent with FN-mediated retention of SA in the shearing junction, which (i) promotes faster aggregation due to higher number of SA and FN molecules (in unfolded conformation) available for aggregation and (ii) prevents SA-FN aggregates from rolling out of the junction due to remaining strong interactions between unfolded FN and mica (absent in ‘SA-only’ systems) [3].

Denatured/decomposed protein deposits have been previously identified on the bearing surfaces of recovered metal-on-metal implants, and local shear stresses were proposed as the mechanism of this protein decomposition, either via a direct ‘mechanical’ effect on protein structure or via an indirect ‘thermal’ effect associated with shear-induced temperature raise within the shearing junctions [4].

4.2 Effect of Shearing Parameters:

4.2.1 Initial Abrupt Film Thickening and Aggregates Formation:

As mentioned above, under shear, FN+SA films form numerous, dense, long-lived aggregates likely composed of intertwined (denatured) FN and SA molecules. These fast-forming aggregates grow and/or coalesce with time of shear. Because aggregate formation was associated with both an initial abrupt film thickening ΔD and a more gradual increase in film

thickness under prolonged shear, which all differed upon shearing conditions (Protocols), in this section we discuss these variations in film thickening. To facilitate the discussion, we refer to figure 3.1.3 which summarizes the abrupt film thickening ΔD measured during Protocols 1, 2, 3, and 4 when shearing at low loads. Here, we should recall that, although we varied both shear amplitude (5Vpp or 20Vpp) and shear frequency (0.0125Hz, 0.05Hz, or 0.2Hz), P1 and P2 had same low shear velocity (V_{shear} = 0.875 μm/s) while P3 and P4 had same high shear velocity (V_{shear} = 3.5 μm/s).

The most obvious observation is that $\Delta D_{P3}$was the highest of all, followed by ΔD_{P4}, ΔD_{P2} and ΔD_{P1}. This result indicates that shear velocity may play a key role in initial film thickening. Furthermore, our statistical analysis showcases that shearing cycles and shearing amplitude were statistically significant, i.e., ΔD did significantly depend on both. The contour plot (Fig. 3.5.2) clearly showcases the effects of these variables on the mean predicted value of ΔD by the regression model. ΔD predicted values seem to be the highest when shearing amplitude was the highest while shearing cycles lowest. However, although both P3 and P4 have identical velocities, ΔD_{P3} is significantly higher than ΔD_{P4}, suggesting that abrupt film thickening is more sensitive to shearing amplitude. Hence it seems that the film needs to be sheared both above a critical velocity V_c and above a critical amplitude A_c to exhibit abrupt thickening at the onset of shear. The trend obtained at low velocity for P1 and P2 confirms this hypothesis and tends to emphasize the even bigger role of shear amplitude since for each V_{shear} tested, ΔD was higher when shear amplitude was higher ($\Delta D_{P2} > \Delta D_{P1}$ and $\Delta D_{P3} > \Delta D_{P4}$). Here the shear-mediated film thickening was attributed to the combination of aggregate formation (as discussed in detail below) and entrance of new, uncompressed and unsheared SA molecules from the liquid reservoir that surrounds the sheared junction, and previously used to incubated the mica surfaces.

To facilitate our discussion about aggregate formation associated with above mentioned abrupt film thickening, here we refer to Table 3.1.2, which summarizes all shearing data responsible for aggregate formation in each Protocol tested, i.e., total shearing time, total number of shearing cycles, and cumulative distance sheared till aggregates start forming in the junction.

Not only P3 test had the highest ΔD but it was also in P3 experiments that aggregates formed first. This result indicates that abrupt film thickening (i.e., initial separation between sheared surfaces) and aggregates formation are linked and that the shearing conditions responsible for aggregation are likely similar to those leading to initial high surface separation.

Indeed, we can see that there likely exist both (i) a minimum shear amplitude A_c required for aggregates formation since P1 does not form aggregates while P2 does (both have same V_{shear} but different shear amplitude), and (ii) a required minimum shear velocity V_c since P4 is able to form aggregates when P1 cannot although they have the same low amplitude but different V_{shear}. Additionally, when comparing P2 and P3, which can both form aggregates while having same amplitude (20Vpp) but different velocity, it seems that the onset of aggregate formation might be roughly proportional to the product of total distance sheared by shear velocity, i.e., the lower is the velocity, the larger is the distance needed to be sheared (and vice versa) to induce aggregation.

The idea that shearing amplitude is an influential factor in the formation of agglomerates has been previously proposed by C. Drummond *et al.* in their SFA study of branched hydrocarbons [5]. Although in our study, the sheared system is structurally different since SA is initially a heart-shaped molecule, it has been shown that SA denatures under shear [6], losing its initial (rather globular) conformation to become more stretched/elongated. Such molecular changes are enhanced by the presence of FN, which also denatures and unfolds upon shear to entangle with SA. Therefore SA-FN aggregation could be more sensitive to amplitude sheared (with respect to diameter of contact between surfaces) rather than shear velocity, as new molecules entering the contact need to be confined and sheared over a sufficient (critical) distance to be unfolded/stretched before being able to interact with their unfolded/stretched neighbour and form aggregates.

Furthermore, our statistical analysis (ref. section 3.5.3) suggests that the formation of aggregates is more sensitive to shear amplitude than to shearing cycles. When multiple regression analysis was carried out on aggregate shearing cycle values with shearing amplitude and shearing cycles as controlled variables, it was clearly seen that aggregate shearing cycles significantly depended on the former than the latter. The main effects plot for aggregate shearing cycles (Fig. 3.5.4) also indicates that when shearing amplitude is increased, the predicted mean shearing cycles decreases, i.e., the larger the amplitude, the lesser number of shearing cycles is needed for FN+SA film to form aggregates. However, our data do not allow us to correlate number of shearing cycles with total shearing time (which depends on V_{shear}), as only one experiment was performed in the P2 conditions.

4.2.2 Gradual Film Thickening upon Prolonged Shear and Aggregates Maturation:

The abrupt initial film thickening ΔD was systematically followed by a gradual raise in film thickness occurring upon prolonged shear. Such gradual film thickening was observed in

all protocols, even in P1 that did not show any aggregation and in P4 that showed aggregation only after circa half hour of shearing. In the case of P1, this gradual film thickening was therefore attributed to more fluid entering the contact that likely still possessed the same structural properties of the bulk reservoir, and then gradually changed when submitted to confined shear. Note that although no aggregates were visible after more than one hour of shear, the FECO flattened with time (compare Fig. 3.1.4 (A) Left → Right), suggesting that classical elastohydrodynamic lubrication (EHL) deformation could have taken place. In classical EHL, zero slip condition is assumed at the fluid-surface boundary, which could give rise to the characteristic deformations (flattening of FECO) observed. Furthermore, this flattening of FECO was also observed in P2 (compare Fig. 3.1.4 (B) Left → Right). These deformations consequently give rise to a normal stress component, which forces the surface separation to increase. In all other cases, there was no clear sign of EHL deformation, instead a different regime took place, where separation between surfaces slowly increased while the surfaces still adopted a round (undeformed) shape. This regime could be attributed to a thick film lubrication (TFL) regime, in which the bulk rheological properties of the fluid govern the lubrication of the surfaces. This TFL regime is likely associated with a significant viscosity increase in the confined SA fluid with respect to its bulk rheological value, as previously measured by Banquy *et. al.* who reported 5 orders of magnitude increase in viscosity for equine synovial fluid when confined in the shearing junction with respect to the bulk values at similar shear rates [7]. However, this discrepancy in viscosity values suggest that other phenomena take place simultaneously in the sheared junction. In fact, FECO imaging reveals more profound changes in the sheared film that evolves from a dense and highly viscous fluid film, homogeneously distributed in the entire contact, to a heterogeneous mixture composed of 'inhomogeneities' of higher refractive index (seen as ripples on even fringes) surrounding by liquid. This gradually leads to small SA 'particles' (denser than the anchored SA film) forming at the sheared interface, i.e., the dense film/fluid interface due to strong attachment of SA onto mica in presence of FN [8].

As shear is prolonged, these 'particles', a.k.a. aggregates, continue growing at the fluid/fluid interface (only visible on even FECO) till clear local deformations of the mica surfaces become evident on both even and odd FECO (Fig. 3.1.4. (C)). These large FECO deformations and our observation of Newton rings at the end of the shearing session (Fig. 3.1.5) suggest that, as they grew, these initially small and randomly distributed aggregates tended to gradually align and coalesce to form "strings" resulting in large rod-like shaped aggregates,

oriented roughly 45° with respect to the shear direction. These results are in agreement with previously reported shear-alignment of aggregates in sheared synovial fluid [7].

4.2.3 Aggregates Stability and Mobility:

We estimated the longevity of the aggregates formed in both FN+SA and SA films and found that all of them were extremely stable over time. First, we observed that they did not dissolve when the surfaces were immersed back in the reservoir made of dilute SA solution, instead, they subsisted and stayed anchored to the previously sheared surfaces. Second, aggregates were also found to resist to new compression (although flattening was observed upon load increase) and new session of shear between the surfaces. These data confirm that the aggregation process we report is mostly irreversible, which reinforces the idea that aggregates comprise mainly irreversibly bound denaturated proteins.

Although they would not dissolve, we found that aggregates would keep some mobility in the contacting junction, in particular when surfaces would be subjected to another shear session. FN+SA and 'SA only' displayed different mobility, with more obvious (larger) displacements observed via FECO for 'SA only' aggregates in particular from the center to the edge of the junction, while FN+SA aggregates would tend to grow and coalesce. These results confirm that SA films, and associated aggregates formed, are more loosely bound to the confining mica surfaces than FN+SA films, which could lead to pure slippage of 'SA only' aggregates while FN+SA rod-like aggregates would roll (without slippage) at the interface and ensure better lubrication.

4.2.4 Friction, Third Body Lubrication and Damage:

The average friction forces we report in section 3.1.4. for all protocols performed under low applied loads indicate that, amongst all shear conditions tested, P3 displays the lowest friction force and associated friction coefficient ($\mu_{P3} \approx 0.36 \pm 0.05$). As P3 is the Protocol in which aggregates form the fastest (only 35s after shear starts), such low friction is consistent with the shear-induced formation and growth of aggregates in the contact. The growth mechanism is similar to a snowball mechanism where new SA molecules (and FN) continuously adsorb onto initially small aggregates as they are displaced in the contact, leading to large rod-like shaped aggregates that ensure rolling friction and large separation (nearly 130 nm, as seen in Fig. 3.1.2 (C)) between sheared surfaces. This leads to gradually decreasing friction (as observed for P3 in Fig. 3.1.6 (C)) and ensure absence of damage of the sheared surfaces, even under prolonged shear and higher load applications. As previously reported for sheared soft contacts, the existence of rolling friction, often also called third body lubrication,

has important implications for joint lubrication as it systematically decreases frictional forces and prevents surfaces to come in to close contact even if the lamina splendens gel layer has been damaged locally [9].

The above-mentioned mechanism can also explain the friction behaviour of P4, which also exhibits a decrease in friction after aggregates start forming in the contact. However, FECO and Newton rings suggest that the aggregates are smaller than in the case of P3 and stay randomly distributed in the contact instead of coalescing into larger rod-like shaped aggregates. As a consequence, the separation between surfaces only increases up to circa 70 nm (Fig. 3.1.2. (D)), which prevents damage but does not allow pure rolling low friction as in the case of P3.

The friction forces and associated friction coefficients were the highest for P1 and P2, which were also the Protocols in which the sheared velocity was the lowest. As already mentioned in section 4.2.2, the viscosity within the confined films (before aggregate formation) is likely orders of magnitude higher than that of the corresponding bulk films at similar shear rates, additionally, shear thinning was reported for thin films of synovial fluid sheared between rigid mica surfaces [7]. This decrease in viscosity with shear rate (hence shear velocity) could explain the higher friction measured for P1 and P2 (V_{shear} = 0.875 μm/s) with respect to P3 and P4 (V_{shear} = 3.5 μm/s). This effect is enhanced with the transformation of a homogeneous dense and highly viscous SA films (P1) showing high friction to a composite fluid film made of native SA fluid and SA-FN aggregates (P3, P4) showing third body low friction.

The peculiar case of P2, which is able to form aggregates but still shows quite high friction, could be explained by the large distance sheared. As reported by Drummond *et. al.* for branched hydrocarbons, as long as the shearing distance/amplitude is above a critical value (which is the case here), the lower the velocity, the longer the time needed by molecules to get stretched/aligned in the contact, as shear/mechanical factors are now competing with thermal entropic factors that tend to keep them in a more disordered configuration. The alignment of the molecules will decrease the force required for sliding the surfaces at a constant rate while the thermally induced disorder will have an opposite effect. However, in our P2 case, even though V_{shear} is low, the 20 Vpp amplitude (corresponding to a shearing distance of circa 35 μm) is high enough to drag/stretch new SA molecules entering the contact and start aggregation in the film. In contrast, in our P1 case (same low V_{shear}), the 5 Vpp sheared amplitude (corresponding to a distance of circa 17.5 μm) is too small to get the same effect, as it is much smaller than the size of the sheared junction.

Importantly, despite differences in friction values and presence/absence of aggregates in the contact, none of the shearing conditions tested in our experiments led to surface damage, which demonstrates the remarkable surface protective abilities of SA films.

In our previous study, we had used protocol P3 to test the shearing behaviour of FN+SF, FN+HA, and FN+LUB, apart from FN+SA [8]. It was reported that while FN+SA and FN+HA initially displayed similar coefficients of friction as compared to FN+SF, friction increased with prolonged shearing for FN+SA and FN+HA, while it remained stable for FN+SF. Coefficient of friction for FN+LUB, however, was lower than FN+SF at the initial stages, but it too was reported to display an increasing trend in its friction over prolonged shearing. The increase in friction for both FN+HA and FN+LUB was attributed to the depletion of their film thickness, i.e. the film getting expelled from the contact junction, over time. It should be noted that although all showcased formation of aggregates upon shearing, one of the main differences observed between these proteins was surface damage. While, FN+SA and FN+SF did not report any damage to the underlying mica surfaces, FN+HA on the contrary showed damage on the FECO. Our FN+SA results were in agreement with those reported in the above-mentioned study [8].

4.3 Effect of Applied Load:

4.3.1 Film Thickness Transient Behaviour and SA aggregation:

Although we only performed high load experiments using P1 protocols (i.e., no aggregate conditions and low load shear followed by high load shear on the same position), we observed both expected and unexpected, more interesting, phenomena. As expected, increasing load led to a decrease in overall film thickness and to a smaller initial film thickening ΔD when shear was resumed. The overall lower film thickness (with respect to that of films subjected to low load) was attributed to weekly bound or free SA molecules being expelled from the contact, however, the presence of FN could ensure that a circa 20 nm SA film was still confined between surfaces prior to high load shear. The smaller initial film thickening $\Delta D_{High} = 5$ nm (with respect to $\Delta D_{Low} = 21.5$ nm) was attributed to a restricted influx of new SA material from the surrounding reservoir due to higher load and initially thinner junction. This effect could also be the result of increased molecular density in the highly compressed film.

Interestingly, in all high load experiments that followed low load shearing, a temporary bulging effect was observed in the central region of the FECO, which was concomitant with the increase in load and the onset of the new shearing session (Fig. 3.2.3). This bulge is the

result of the elastic deformation of the mica surfaces due to a heterogeneous distribution of the molecules in the confined film. Here, a thick and dense film portion was trapped in the central region of the contact, corresponding to the previously sheared area that would comprise already aligned/stretched molecules, while a less dense and thinner film portion was located at the edges of the contact, corresponding to newly compressed molecules not yet aligned/stretched. Under prolonged shear, this bulge gradually disappeared and the overall film thickness slowly increased (as visible through FECO flattening and right shift), which indicates a large contact area confining a thick and dense homogeneously distributed film that comprises mostly shear-aligned/stretched molecules.

Additionally, as no aggregation was observed after shearing one hour at low load followed by one hour at high load, our results suggest that neither load nor shear time affect the transition responsible for aggregation of SA molecules, as long as both shear amplitude and shear velocity are below the critical values mentioned earlier. Instead, these findings reinforce the idea of the preponderant role of a minimum sheared distance required for aggregation with respect to the diameter of contact of the junction, as here, increased load leads to increased contact diameter of the SFA junction (due to glue deformation below the mica) hence an even larger shear amplitude would be expected to shear-align molecules entering this larger junction.

4.3.2 Friction Under High Normal Loads and Damage:

As expected, the friction force increased with applied load, however it seems that the friction coefficients slightly decreased with applied load from $\mu_{Low} = 0.45$ to $\mu_{High} = 0.35$. Here we should point out that the friction coefficients measured in our experiments are notably higher than the values reported in previous SFA experiments on isolated SF components [2]. One key difference is that the data presented here are instantaneous measurements calculated for each shearing cycle under constant load while previous studies have typically reported average friction coefficients measured under incrementally increasing loads [2]. This may clarify the incongruity in friction coefficient and explain why Amonton's law does not seem to apply although the film stays in a fluid state and no aggregate or damage occurred during our entire experiments.

Indeed, as no aggregates were formed and no increase in coefficient of friction was measured, our high load shearing results confirm that SA films display excellent surface protection against wear (at low velocity) even when films are confined under high pressure and sheared over longer times than those described in the previous sections.

4.4 Effect of Previous Shear History:

In this approach, we compared previously sheared FN+SA and 'SA only' films by monitoring the mobility of the aggregates formed when shear was resumed after a separation time and distance between the shearing surfaces. Although we observed a clear growth of FN+SA aggregates, 'SA only' aggregates tended to saturate in size and/or to be easily displaced in the sheared junction (Figs. 3.4.2 (A) and (B)). This shear-mediated growth mechanism was previously reported by Banquy and coworkers as "rolling snowball" mechanism, where small existing agglomerates would get bigger as new SA fluid molecules (and FN in our case) would adsorb onto them till they become large rod-like agglomerates able to roll in the junction [7]. In absence of FN, 'SA only' agglomerates were not able to grow in size but as they were weakly bound to the underlying surface, they could be easily displaced in the junction from high pressure area (center) to low pressure area (edges). This test establishes a relationship between strength of anchoring of SA molecules with growth dynamics, size, and mobility of agglomerates.

4.5 Extending our Findings to Joint and Implant Lubrication:

On one hand we should point out that the surface of the mica substrates used in all our SFA experiments is atomically smooth, rigid, and non-porous, which makes it structurally and mechanically different from that of cartilage, which is heterogeneous, rough, compliant, and porous. Because of these differences, caution must be used in generalizing our findings beyond rigid surfaces. Nevertheless, using these model surfaces allows us to evaluate accurately the structure-tribology relationship of thin lubricating films by ensuring that all shear-induced events measured can be attributed to changes in the interfacial lubricant, i.e., to phenomena occurring at the junction *between* surfaces rather than *within* surfaces. Our results are therefore applicable to other tribosystems involving rigid surfaces, in particular most artificial joints.

On the other hand, although articular joints are complex multi-component systems and therefore difficult to model at the molecular level, our SFA approach could also be seen as a way to reduce such complex tribosystem to a 'single asperity' whose dimensions would be similar to those found in cartilage. Typically, surface asperities in cartilage have a height of 1–10 μm and a mean distance between asperities from 1–50 μm [7]. Under pressure, these asperities are expected to deform and reach a contact area of 20 to 100 μm in diameter, which are exactly the geometrical characteristics of the 'single asperity' junction that can be attained with the SFA using mica surfaces as model surfaces. Hence the advantage of using mica is that,

in contrary to the cartilage surface, any shear-induced changes in the interfacial fluid between contacting asperities can be accurately observed.

In this context, the formation of large and long-lived aggregates associated with the efficient surface protection we observed in SA films indicates that globular proteins may play a prominent role in the aggregation phenomena previously reported in the literature for synovial fluid. Additionally, while the formation of aggregates in synovial fluid and the development of wear-protecting "protein gels" in fetal bovine serum (FBS) had been previously observed in separate studies, our findings correlate both phenomena by suggesting that SA aggregation and surface protection against damage are intimately connected, and that this connection might be at the heart of the highly efficient lubrication of synovial fluid. Our results are applicable to various rigid systems such as artificial joints, in which the dynamic aggregation of SA may play a pivotal lubricating role by providing an 'on demand' wear protecting protein cushion in response to high normal loads and shear stresses. Although it will be of future interest to investigate SA aggregation between cartilage-mimicking surfaces to elucidate its role in natural joints, the identification of a self-replenishing, shear-induced lubricating mechanism mediated by the aggregation of globular proteins advances our current understanding of joint implants' lubrication with implications for future design and therapeutic interventions.

Therefore, our technique could be used for systematic characterization of adsorption, aggregate formation, and lubrication of protein films on a variety of implant materials with different surface properties to advance our understanding of structure-function relationship of protein films and improve both the design and the materials properties of artificial joints.

4.6 References:

[1] Heuberger, M. P.; Widmer, M. R.; Zobeley, E.; Glockshuber, R.; Spencer, N. D. Protein-Mediated Boundary Lubrication in Arthroplasty. *Biomaterials* **2005**, *26* (10), 1165–1173.

[2] R. C. Andresen Eguiluz, S. G. Cook, C. N. Brown, F. Wu, N. J. Pacifici, L. J. Bonassar, and D. Gourdon, "Fibronectin mediates enhanced wear protection of lubricin during shear," *Biomacromolecules*, vol. 16, no. 9, pp. 2884–2894, 2015.

[3] M. Hindié, E. Camand, R. Agniel, F. Carreiras, E. Pauthe, and P. Van Tassel, "Effects of human fibronectin and human serum albumin sequential adsorption on preosteoblastic cell adhesion," *Biointerphases*, vol. 9, no. 2, p. 29008, 2014.

[4] K. M. . Oates, W. E. Krause, R. L. Jones, and R. H. Colby, "Rheopexy of synovial fluid and protein aggregation," *J. R. Soc. Interface*, vol. 3, no. 6, pp. 167–174, 2006.

[5] C. Drummond and J. Israelachvili, "Dynamic behavior of confined branched hydrocarbon lubricant fluids under shear," *Macromolecules*, vol. 33, no. 13, pp. 4910–4920, 2000.

[6] H. Mishina and M. Kojima, "Changes in human serum albumin on arthroplasty frictional surfaces," *Wear*, vol. 265, no. 5–6, pp. 655–663, 2008.

[7] X. Banquy, D. W. Lee, S. Das, J. Hogan, and J. N. Israelachvili, "Shear-induced aggregation of mammalian synovial fluid components under boundary lubrication conditions," *Adv. Funct. Mater.*, vol. 24, no. 21, pp. 3152–3161, 2014.

[8] S. G. Cook, Y. Guan, N. J. Pacifici, C. N. Brown, E. Czacko, M. S. Samak, L. J. Bonassar, and D. Gourdon "Dynamics of Synovial Fluid Aggregation under Shear," in revision at *Langmuir* (Special issue Intermolecular Forces and Interfacial Science), 2019.

[9] Murakami, T., Sawae, Y., Nakashima, K., Yarimitsu, S., & Sato, T. (2007). Micro- and nanoscopic biotribological behaviours in natural synovial joints and artificial joints. *Proceedings of the Institution of Mechanical Engineers, Part J: Journal of Engineering Tribology*, *221*(3), 237–245.

Chapter - V : Conclusions and Future Directions

Current approaches that seek to elucidate the remarkable lubrication of synovial fluid usually focus on the roles of hyaluronic acid and lubricin and frequently overlook the role serum albumin (SA) although it represents 90% of the protein content of synovial fluid. In this thesis, we used the Surface Forces Apparatus to investigate in detail the structural and tribological response of SA thin films when sheared between model mica surfaces and subjected to a large range of shearing parameters.

Our data indicate that, when they are sheared, SA films are able to replicate the transformation previously reported for synovial fluid, i.e., abrupt film thickening and formation of numerous long-lived aggregates accompanied by low friction and efficient surface protection against damage. More specifically, our investigation of multiple shear parameters reveals that:

(i) Strong anchoring of SA to shearing surfaces not only accelerates aggregation but also promotes the formation of stiffer aggregates that enable efficient rolling friction (third body lubrication), which keeps surfaces apart and ensures prevention against damage.

(ii) The aggregates formed are likely the result of shear alignment, shear stretching of denaturated SA molecules that have lost their initial globular conformations, i.e., have unfolded due to combined mechanical and thermal effects. Such aggregation mechanism is therefore largely irreversible, which makes aggregates very stable and long-lived in the contact.

(iii) Although more experiments are needed to deconvolute the individual roles of some parameters tested, aggregate formation only occurred when SA was sheared above a 'critical' amplitude A_c and a critical shear velocity V_c. Consequently, neither the pressure applied nor the time of shearing could affect aggregation, as long as those 'critical' conditions were not satisfied.

Collectively, our results provide experimental evidence of the role of globular proteins, such as SA, in a process of self-replenishing, shear-induced lubricating mechanism and establish a correlation between shearing parameters, formation and stability of aggregates, low friction and efficient wear protection. Although our findings are based on experiments involving rigid, nonporous surfaces hence can hardly be generalized to compliant and porous cartilage surfaces, they are applicable to other rigid tribosystems such as artificial joints and

will certainly advance our understanding of joint implants' lubrication in synovial fluid mediated by protein aggregation, with implications for future design of artificial joints and therapeutic interventions.

Regarding SA lubrication, further studies are needed to deconvolute the individual and/or cooperative roles of sheared amplitude/distance and shear velocity in SA response to shear. The ratio between sheared amplitude and diameter of contact of the sheared junction also seems critical and should be investigated, as it defines a correlation between total number of molecules under confinement, flux of new molecules entering the shearing junction, and distance needed to stretch/shear-align them and form aggregates. Also, as it is clear from our experiments that the strength of attachment of SA to surfaces is a key contributor to aggregates size, composition and mechanics, more experiments are needed to investigate the actual role(s) of fibronectin and its denaturation. To do so, a different protocol should be used to anchor SA to mica (grafting, sputtering) and more accurate techniques should be used to characterize the aggregates formed (e.g., systematic refractive index measurements during shear, optical microscopy during shear, atomic force microscopy after shear and freeze drying of the sheared junction). The rheological properties of SA confined in microchannels with or without FN coating would also help clarifying the effect of fluid/fluid and fluid/solid interface and the variations of SA viscosity as a function of shear rate, since both shear-thickening (at low shear rates) and shear-thinning (at high shear rates) have been reported in the literature for various types synovial fluids.

More generally, it has been a long time since synovial fluid proteins have been studied for their role in wear protection and lubricating properties in artificial joints. Shear studies done on implants made of stainless steel, UHMWPE, and alumina showed proteins 'aggregates gels' being adsorbed onto the previously surfaces in varied proportions, which depended on the hydrophobicity and roughness of the surface. This adsorbed layer of proteins displayed surface protective capabilities, minimising the wear of the shearing surfaces thereby increasing the lifespan of the system. Here we present a framework that allows in situ simultaneous measurement of film thickness, film heterogeneities (protein aggregation), friction, and presence of surface damage. Therefore, our technique could be used for systematic characterization of adsorption, aggregate formation, and lubrication of protein films on a variety of implant materials with different surface properties to advance our understanding of structure-function relationship of protein films and improve both the design and the materials properties of artificial joints.

Finally, it is obviously of future interest to investigate SA (and other synovial fluid components) aggregation between cartilage and/or cartilage-mimicking surfaces to elucidate the role of aggregation (if any) in natural joints. As the role of the superficial zone in boundary lubrication, and most particularly the Laminar Splendens (LS) gel layer, is still unclear, investigating the mechanisms at the origin of the formation of the LS and its role in protecting cartilage's fragile surface is fundamental. And it is in the interest of all of us to elucidate if the shear-mediated 'on demand' thickening and particle formation mechanisms observed in this thesis are also occurring in articular joints and play an essential role in their lubrication.

Appendix

Following is a sample calculation for time (s) required to apply a specific force (mN) on the shearing surfaces using the motor:

Speed (S) of the motor ***after*** calibration test:

$$S = 7.5\ nm/s$$

Spring constant (K):

$$K = 1656000\ mN/m$$

Now, force needed to be applied,

$$f = 1\ mN$$

Using Hooke's law,

$$f = Kx$$

Where, x is the distance. Using the values of f and K, finding x

$$x = \frac{1}{1656000}(m)$$

$$x = 6.04 * 10^{-7}(m)$$

Now,

Speed = distance/time (m/s)

$$S = \frac{\text{x}}{\text{time}}(m/s)$$

$$time = {6.04 * 10^{-7}(m)}\Big/{7.5\ (^{nm}/_{s})}$$

$$time \approx 80\ (s)$$

Hence, to apply 1 mN of force with the motor speed of 7.5 nm/s, the time needed to keep the motor running is approx. 80 seconds.

I would like to mention that Figures 1.1.2 and 1.4.1 were referenced in this thesis after taking prior permission of the respective authors.